



HAL
open science

Li and Si isotopes reveal authigenic clay formation in a palaeo-delta

Xu (Yvon) Zhang, Jérôme Gaillardet, Laurie Barrier, Julien Bouchez

► **To cite this version:**

Xu (Yvon) Zhang, Jérôme Gaillardet, Laurie Barrier, Julien Bouchez. Li and Si isotopes reveal authigenic clay formation in a palaeo-delta. *Earth and Planetary Science Letters*, 2022, 578, pp.117339. 10.1016/j.epsl.2021.117339 . hal-04349544

HAL Id: hal-04349544

<https://hal.science/hal-04349544>

Submitted on 18 Dec 2023

HAL is a multi-disciplinary open access archive for the deposit and dissemination of scientific research documents, whether they are published or not. The documents may come from teaching and research institutions in France or abroad, or from public or private research centers.

L'archive ouverte pluridisciplinaire **HAL**, est destinée au dépôt et à la diffusion de documents scientifiques de niveau recherche, publiés ou non, émanant des établissements d'enseignement et de recherche français ou étrangers, des laboratoires publics ou privés.

1 **Li and Si isotopes reveal authigenic clay formation in a palaeo-delta**

2 Xu (Yvon) Zhang^{a, b}, Jérôme Gaillardet^a, Laurie Barrier^a, and Julien Bouchez^a

3 ^a *Université de Paris, Institut de Physique du Globe de Paris, CNRS, Paris, 75005, France*

4 ^b *Institut Terre et Environnement de Strasbourg, Université de Strasbourg, CNRS, 5 rue René*
5 *Descartes, 67084 Strasbourg Cedex, France*

6 **ABSTRACT**

7 Marine authigenic clay formation has long been postulated as a major process
8 to explain the mass budgets of some elements in seawater, and might act a reverse
9 reaction for the neutralization of atmospheric acidity by soil forming reactions on land.
10 Nevertheless, to date, a handful of studies have directly investigated the effect of
11 reverse weathering due to the challenges associated with sampling complexity. Deltas
12 are thought to be one of the possible environments where reverse weathering reactions
13 may occur because of the abundant influx of weathering derived materials and dynamic
14 activities. In this study, we use a unique combination of three isotope systems (Si, Li,
15 and Nd) as evidence of authigenic clay formation using sediments collected from a ~40
16 Ma-old delta complex (Ainsa Basin, Spain). Sediments were collected along the land
17 to sea depositional continuum, from alluvial and coastal plains to marine environments.
18 Direct comparison between alluvial, coastal, and marine sediments allows for observing
19 the potential effect of reverse weathering. Systematic differences in Si and Li isotope
20 composition exist between marine and continental sediments, revealing the formation
21 of an authigenic phase sequestering light Li and Si as associated with the diagenesis of
22 Fe in reducing deltaic environments. Finally, this study proposes a geochemical tool for
23 helping distinguishing marine and continental origins of sedimentary rocks when
24 lithofacies and biofacies prove to be ineffective.

25

26 **Key words**

27 Reverse weathering, Li isotopes, Si isotopes, authigenic clays, delta, marine chemistry

28 **1. Introduction**

29 The changes in chemical composition of seawater over geological time witness
30 the co-evolution of input fluxes to the ocean by rivers or seafloor hydrothermal
31 activities and of output fluxes such as secondary mineral precipitations, *i.e.* as
32 carbonates or authigenic clay formations (Holland, 2005). The pioneering work of
33 Mackenzie and Garrels (1966) postulated the existence of so-called “reverse weathering”
34 processes in the ocean, acting as back reactions of silicate weathering on terrestrial
35 surfaces (Michalopoulos and Aller, 1995). During reverse weathering in the marine
36 environment, authigenic clay formation not only takes up cations, but it also consumes
37 alkalinity, releases CO₂ to the ocean-atmosphere system, modifies the ocean pH,
38 thereby impacting the geological carbon cycle (*e.g.* Isson et al., 2020; Isson and
39 Planavsky, 2018; Sillen, 1967). This reverse weathering hypothesis is however
40 challenging to test as the products of reverse weathering are difficult to identify in
41 contemporary marine sediments which are overwhelmed by complex mixtures of
42 terrigenous and biogenic particles. As a consequence, in contrast with silicate
43 weathering fluxes occurring on terrestrial surfaces, cations fluxes involved in reverse
44 weathering reactions at the global scale are still poorly known. In addition, it is still
45 unclear where does reverse weathering occur (coastal margin or in deep-sea sediments)
46 and how it is affected by different geological settings.

47 Experimental studies using major elements and microscopy techniques have
48 shown that coastal environments (deltas and estuaries) are viable candidates as sites for
49 reactions scavenging terrestrially-derived cations through early diagenesis in the

50 sediment column (Michalopoulos and Aller, 2004, 1995). Recently new approaches
51 using stable and cosmogenic isotopes have identified reverse weathering reactions and
52 offer the promise to better constrain the fluxes associated with reverse weathering
53 reactions (*e.g.* Andrews et al., 2020; Bernhardt et al., 2020; Rahman et al., 2016;
54 Santiago Ramos et al., 2020; Zhang et al., 2021).

55 Among the non-traditional stable isotopes, Li isotopes have proven good
56 proxies of reverse weathering reactions due to the affinity of Li for secondary minerals
57 and because the two isotopes of Li, ^6Li and ^7Li , are discriminated during their
58 coprecipitations in clays. Studies conducted in modern estuaries and pore fluids of
59 marine sediments (Andrews et al., 2020; James and Palmer, 2000; Pogge von
60 Strandmann et al., 2008) have reported significant isotopic variations. Constraints on
61 the global Li cycle suggest an outflux of Li from the ocean balancing the influx from
62 weathering and hydrothermal processes. The uptake of seawater Li by the formation of
63 authigenic clays during reverse weathering is a strong candidate for such a flux (Li and
64 West, 2014; Misra and Froelich, 2012). In the critical zone (soil, rivers, groundwaters),
65 the Li isotope signature appeared to be a powerful tracer for the formation of secondary
66 minerals in soils or floodplains (*e.g.* Dellinger et al., 2017, 2014; Golla et al., 2021;
67 Huh et al., 1998), and a good proxy for distinguishing modern products of chemical
68 weathering (pedogenic) from ancient marine sedimentary rocks (Dellinger et al., 2014).
69 Reverse weathering processes could enrich Li and shift the isotopic composition of
70 continental derived solid weathering products toward a ^7Li enrichment (Teng et al.,
71 2004). River study in the Amazon and Mackenzie basins have revealed that river
72 sediments derived from the weathering of a marine sedimentary reservoir clearly appear
73 to be enriched in Li and isotopically lighter than the modern solid weathering products
74 derived from granitic rocks (Dellinger et al., 2014). This modification of Li

75 geochemistry in marine sediments compared to their continental counterparts can occur
76 during early or burial diagenesis processes, and in a variety of environments from
77 estuarine and deltaic zones to the open ocean and within the sedimentary pile.

78 Although studying modern coastal depositional systems to quantify reverse
79 weathering is the simplest approach to understand early diagenesis processes, it suffers
80 from several issues, chiefly (1) the difficulty of isolating the sediment from seawater or
81 porewater without altering the sediment composition, and (2) limitations encountered
82 when trying to explore the long-term effect of a process studied over relatively short
83 timescales.

84 Here as an alternative, we turn to a geological analogue to circumvent these
85 difficulties. We investigate the Tertiary Ainsa palaeo-delta system in Spain (Fig. 1), a
86 sedimentological system that has been the object of a breadth of studies aiming at
87 understanding the links between active tectonics and deltaic sedimentary facies and
88 architecture (*e.g.* Caja et al., 2010; Dreyer et al., 1999; Pickering and Bayliss, 2009;
89 Pickering and Corregidor, 2005). This foreland delta was formed during the Eocene, 43
90 Ma, by the accumulation of erosion products from the then-forming Pyrenees. Refined
91 sequence stratigraphy works have characterized the alluvial, coastal, and marine
92 components from the geometrical and petrological points of view (Dreyer et al., 1999).
93 The advantage of focusing on a palaeo-delta sedimentary series is that it offers a
94 spatially (~1 km) and temporally (~1 Myr) integrated view of the effects of deltaic
95 processes. Although such an approach is associated with potential challenges including
96 sediment preservation and uncertainties about palaeo-seawater chemistry, it allows for
97 probing authigenic effects directly by comparing the marine and continental sediments
98 deposited within a relatively limited time window. To our knowledge, this study is the
99 first investigation of reverse weathering reactions in a palaeo-deltaic system. Our

100 investigation provides significant evidence for authigenic clay formation in seawater-
101 contacted (marine and coastal) environments.

102 **2. Methods**

103 **2.1 Field description and sampling strategy**

104 Samples were collected in the palaeo-deltaic system of the Ainsa Basin (San
105 Vincente, Sobrarbre, and Escanilla formations; Dreyer et al., 1999), which is part of the
106 Southern Pyrenees foreland basin system (Fig. 1A). This well-studied geological object,
107 formed during the Eocene (from middle Lutetian to early Priabonian), is a natural
108 laboratory to compare sedimentary rocks of roughly the same age (albeit deposited
109 within several Myr), mechanically sorted by sediment transport, and deposited along a
110 land-to-sea (hence salinity) continuum. Palaeogeographic reconstructions indicate that
111 the Ainsa Basin developed between the two N-S Mediano and Boltaña anticlines (Fig.
112 1B). To the south, it is bordered by the Sierras Marginales thrust front. Source material
113 was derived from the then-forming Pyrenees mountain which supplied terrigenous
114 silicates and carbonates to the deltaic system (Caja et al., 2010; Dreyer et al., 1999).
115 Palaeoclimate reconstructions suggest a tropical to subtropical climate with high
116 rainfalls (Pickering and Corregidor, 2005). The relative seawater level varied during
117 basin filling due to local tectonics, as well as glacio-eustatic seawater fluctuations
118 (Dreyer et al., 1999; Pickering and Bayliss, 2009).

119 Based on a field analysis of the lithology and sedimentary structures, one or
120 several sampling sites were chosen (Fig. 1B and 1C) for each of the main sedimentary
121 environments composing the palaeo-deltaic system of the Ainsa Basin (facies as
122 defined in Bhattacharya, 2006): the alluvial plain (for the upstream alluvial plain and
123 upper delta plain, samples with prefix SA), the coastal plain (for the lower delta plain,

124 samples with prefix SC), the delta front (samples with prefix SD), and the prodelta
125 (samples with prefix ST). At these sites, deposits with different grain sizes (from micro-
126 conglomerates to claystones) were sampled in order to access the whole spectrum of
127 terrigenous sediments. Examples of sedimentological sections representative of the
128 deposits of the different environments, and of how they were sampled, are shown in
129 Fig. S1. At each site, 4 to 15 unweathered rocks of different grain size were collected,
130 generally along road cuts. During the sampling, the outermost part of each sample was
131 discarded to eliminate any potential effects of present-day weathering. In the field, the
132 colours of the different outcrops were observed to be distinct: alluvial deposits
133 generally exhibit a red colour, typical of oxidized environments, whereas marine
134 deposits show a greyish colour, typical of sediments formed in reducing environments.
135 Detailed information on each sample is listed in Table S1.

136 **2.2 Sample preparation, concentrations of major and trace elements in bulk** 137 **siliciclastic sediments, and isotope measurements**

138 Thin sections of selected samples were prepared for optical inspection. Then all
139 the collected samples were dried at 50°C and crushed using an agate mortar. Major
140 elements were measured at SARM (Service d'Analyse des Roches et des Minéraux,
141 Vandoeuvre-les-Nancy, France; details of sample preparation analysing methods are
142 provided at <http://helium.crpq.cnrs-nancy.fr/SARM/pages/roches.html>). For trace
143 elements, approximately 0.1 g of the crushed sample powders were dissolved using an
144 HF-HNO₃ method (Dellinger et al., 2014). Trace element concentrations were
145 measured at the Institut de Physique du Globe de Paris (IPGP), using Inductively
146 Coupled Plasma Quadrupole Mass Spectrometry (ICP-Q-MS).

147 Different powder aliquots were used for measuring Si, Li, and Nd isotopes on
148 Thermo Fisher Neptune Plus MC-ICP-MS (See supplementary materials S1.1-S1.3 for

149 the methods used for isotope measurements). Sequential extractions of Li pools were
150 performed on selected samples to better constrain the controls on the bulk Li isotope
151 composition of the samples. In the “rinsing” experiments, each sample was rinsed with
152 Milli-Q water (MQ) by repeating the same procedure three times: (1) First, 5 ml MQ
153 water were added to ~1 g sample which was then shaken vigorously for 24 hours; (2)
154 Then, the sample mixture was centrifuged at 4400 rpm and the top 4 ml solution were
155 pipetted out and filtered at 0.2 μm ; (3) Finally, another 4 ml MQ were added into the
156 residual. Additionally, in a separate set of “leaching” experiments, the same previous
157 protocol was applied, but with 0.5 N HCl instead of MQ. The rinsing and leaching
158 solutions were analysed for Li concentration and its isotope composition. We
159 emphasize that the water rinsing and HCl-leaching experiments were carried out on
160 separate aliquots of sediment samples. Therefore, the first HCl leaches likely include
161 solutes that could have been released during the water rinsing experiment. Due to the
162 challenges associated with separate Si between biological and non-biological Si pools
163 and to detection limits of Si measurements, no extraction experiment was conducted
164 for Si.

165 **3. Results**

166 **3.1 Texture**

167 We selected samples from alluvial, coastal, and marine deposits of various grain
168 sizes (from coarse sandstones to fine siltstones) for mineralogical observations on thin
169 sections by optical microscopy. Representative pictures are shown in Fig. S2 and the
170 associated observations are summarized in Table 1. Overall, the thin sections show that
171 source rocks of the sandstones and siltstones deposited in the Ainsa Basin are a mixture
172 of igneous (among which metamorphic) and sedimentary rocks. These deposits are

173 mainly composed of subangular detrital quartz and carbonates (from crystalline,
174 bioclastic, and micritic limestones), together with minor detrital feldspars, micas,
175 recycled sandstones, and siltstones. In addition, detrital oxides or hydroxides are also
176 common in many samples of the alluvial plain, coastal plain, and prodelta deposits. On
177 the other hand, carbonated bioclasts such as benthic foraminiferas and echinoderm
178 remains are also present in the coarse-grained sediments of the delta front. Between
179 those particles, a calcite cement is visible in the coarse- and medium-grained sandstones
180 of all environments, while a clayey matrix can be observed in the fine-grained
181 sandstones and siltstones. Eventually, micrite can also be observed in the finer-grained
182 samples of the delta front and prodelta deposits.

183 **3.2 Major and trace elements**

184 The major and trace element data are reported in Table S2 and S3, respectively.
185 Grain size exerts a major control on the chemistry of sediments as revealed by the
186 chemical composition of river sediments (*e.g.* Bouchez et al., 2011a). Al/Si ratio can
187 be used as a surrogate for sediment grain size (Bouchez et al., 2011b; Dellinger et al.,
188 2014). The Al/Si ratios of the Ainsa samples range from 0.10 (quartz-rich samples) to
189 0.44 (clay-rich samples), similar to those observed in modern suspended river
190 sediments (Dellinger et al., 2014). In order to correct the grain size effects (such as the
191 dilution effect of quartz, carbonates, and other potential components in the bulk sample;
192 Dellinger et al., 2014), elemental ratios normalized to Al (X/Al) are reported for major
193 elements (Fig. 2A ranked by increasing X/Al ratios from Mn to Ca) and a number of
194 trace elements (Fig. 2B, ranked by increasing X/Al ratios from Cs to Sr) for different
195 sample groups. Within the variability of each sample groups, major and trace elements
196 do not show significant differences between alluvial, coastal and marine environments.
197 Among major elements, only Fe and Na tend to show slight enrichments in the marine

198 and coastal sediments compared to their alluvial counterparts. It is also interesting to
199 note that K, which has been shown to be sensitive to reverse weathering or diagenetic
200 reactions (*e.g.* Fedo et al., 1995; Michalopoulos and Aller, 1995; Santiago Ramos et al.,
201 2020), is not enriched in the marine deposits at Ainsa. Regarding trace elements, Li is
202 slightly enriched in marine deposits (Fig. 2B). Finally, it is notable that the Li content
203 of sampled sediments is closely correlated to the combined abundance of Al and Fe
204 therein (Fig. S3).

205 **3.3 Li, Si and Nd isotopes and sediment grain size (Al/Si)**

206 $\delta^{30}\text{Si}$, $\delta^7\text{Li}$, and ϵNd were analysed for bulk samples, and their results are
207 reported in Table S1. At Ainsa, grain size displays a strong influence on $\delta^{30}\text{Si}$ and $\delta^7\text{Li}$
208 of sediments, whereas little effect on ϵNd (Fig. 3). ϵNd values range from -10.0 to -11.9
209 and are of typical Western Europe upper crustal values (Nägler et al., 1995). $\delta^{30}\text{Si}$
210 shows different values among samples ranging from -0.7‰ to -0.1‰. The $\delta^{30}\text{Si}$
211 decreases with increasing Al/Si ratio, thus with decreasing grain size, particularly when
212 Al/Si > 0.25. The same relationship is observed in river sediments and in shales (Bayon
213 et al., 2018; Savage et al., 2013). The difference in $\delta^{30}\text{Si}$ among different environments
214 is hardly visible, but seawater-contacted sediments are slightly lighter than the alluvial
215 ones for the higher Al/Si ratios. For example, sediments with $\delta^{30}\text{Si}$ values lower than -
216 0.4‰ can only be found in coastal and marine environments.

217 Li isotope compositions show greater variations from -2.4‰ to 6.9‰ and reveal
218 first that $\delta^7\text{Li}$ is strongly dependent upon grain size as observed in modern-day river
219 sediments (Dellinger et al., 2014), and second that the different sample groups show
220 significant differences in $\delta^7\text{Li}$ with marine sediments having lower $\delta^7\text{Li}$ values
221 ($\delta^7\text{Li}=1.0 \pm 4.4\%$, 2σ) than alluvial ones ($\delta^7\text{Li}=3.9 \pm 3.4\%$, 2σ). The coastal plain

222 samples lie in between ($\delta^7\text{Li}=2.6 \pm 3.8\text{‰}$, 2σ). The negative relationship between $\delta^7\text{Li}$
223 and Al/Si in alluvial sediments is similar (although shifted toward higher values) to
224 what is observed in modern-day river sediments (Dellinger et al., 2014).

225 An enrichment of Li in marine sediments accompanied by a fractionation which
226 favours light Li in these sediments is observed when we compare the $\delta^7\text{Li}$ and Li/Al
227 ratio among different deposits (Fig. 4). The probability densities of Li/Al and $\delta^7\text{Li}$ were
228 estimated using Kernel Density Estimations with programs provided by Pedregosa et
229 al., (2011) and are respectively displayed in Fig. 4. A slight enrichment of Li in the
230 marine sediments can be observed: marine samples have higher Li/Al
231 ($\text{Li/Al}=1.17\pm 0.27\times 10^{-3}$) values compared to alluvial samples ($\text{Li/Al}=1.05\pm 0.26\times 10^{-3}$).

232 The different sediment groups display significantly different $\delta^7\text{Li}$ fingerprints
233 with marine sediments have lighter $\delta^7\text{Li}$ signatures than alluvial sediments. This is first
234 shown by statistical analysis with $p<0.05$ (t-test, two tails) between any two
235 environments and is visually displayed by a gradual decrease of $\delta^7\text{Li}$ values
236 corresponding to the peaks of probability densities from alluvial to marine phase
237 sediments. Namely the probability densities are maximal at $\delta^7\text{Li}$ equals to 2.9 ‰ for
238 alluvial sediments, 1.9 ‰ for costal sediments, and 0.4 ‰ for marine sediments. The
239 difference of $\delta^7\text{Li}$ between marine and alluvial sediments is approximately -3 ‰.

240 **3.4 Sequential extractions of Li pools**

241 Initially, two Li pools (palaeo-seawater and carbonate) from the sediment
242 samples were targeted and expected to be extracted. To access these pools, we have
243 opted for a simple and convenient extraction method, which can provide first-order
244 understanding of the Li pools presenting in the palaeo-delta sediments. We note here
245 that any leachate should rather be envisaged as operationally defined as no chemical

246 extraction protocol is perfect.

247 The first Li pool was extracted from rinsing the sample powder with MQ. This
248 water-rinseable Li pool represents the loosely-bound and possibly surface layer sites Li
249 fractions, presumably containing Li from seawater inclusion and adsorbed Li during
250 clay-seawater interaction in clay minerals (*e.g.* Zhang et al., 2021). Overall, as shown
251 in Table 2, 0.32-0.87% of total Li was rinsed from seawater-contacted samples (marine
252 and coastal), whereas this “rinseable” fraction of Li was 0.17-0.43% in alluvial samples.
253 A first-order observation is thus that the seawater-contacted samples contain more
254 rinseable Li compared to alluvial sediments. This small difference in the rinseable Li
255 fraction between seawater-contacted and alluvial sediments may be attributed to a small
256 seawater influence on the sediments. Except for the alluvial samples that have a too-
257 low amount of rinseable Li, the isotope signature of this rinsed fraction was measured
258 for marine sediments and whose values range from 1.91‰ to 12.84‰.

259 The second Li pool was expected to be Li contained in carbonates. Unlike the
260 water-rinsing experiment, significant amounts of cations were extracted during the
261 HCl-leaching experiments (Fig. S4). In these leachates, the dissolved substances can
262 correspond to cations released from the exchangeable sites (also leached to some extent
263 by MQ), carbonates, oxides, clays, and probably primary minerals. Our approach was
264 thus to use a stepwise HCl leaching procedure, in order to roughly separate the Li from
265 all those pools. In all samples, Ca, which is indicative of carbonates, was significantly
266 extracted during the 3 steps of the leaching procedure, in a consistently decreasing
267 fashion, such that at the end of the leaching experiment, a significant fraction of bulk
268 Ca had been extracted for all samples (~55% to ~100% of total Ca, Fig. S4 and Table
269 S4). In the samples where Ca was significantly extracted (>90%), other metals such as
270 Li, Al, or Fe started to be extracted in the second or third step of the procedure as

271 indicated by the Al/Ca and Fe/Ca ratios, which can be quantitatively indicative of
272 different Li pools (Bastian et al., 2018), in the successive leachates (Table 3). Generally,
273 in the first leachates, the Al/Ca and Fe/Ca ratios are low ($\sim 10^{-6}$ - 10^{-5}) indicating that Li
274 in the first leachates is sourced from a rinseable Li pool and from a carbonate Li pool.
275 In the last leachates, the Al/Ca and Fe/Ca become significantly higher ($\sim 10^{-2}$ - 10^{-1}),
276 suggesting that carbonate was dissolved during the previous leaching steps, and that the
277 Li in the last leachates is sourced from the Al-Fe-associated Li pool.

278 Only the $\delta^7\text{Li}$ compositions of the first (rinseable Li and carbonate-bound Li)
279 and third (Al-Fe-associated Li) leachate solutions were measured (Table 3). The $\delta^7\text{Li}$
280 compositions in the first leachates were characterized by values close to or heavier than
281 the bulk $\delta^7\text{Li}$, whereas the $\delta^7\text{Li}$ of the last leachates were characterized by values lighter
282 than the bulk $\delta^7\text{Li}$ (Fig. S5). The leaching results of sample SD7 seem to be opposite to
283 observations from other samples, which we attribute to the low carbonate content in
284 this sample. In sample SD7, the Al-Fe-associated Li was most likely released “earlier”
285 (*i.e.* during the first leaching step) than in other samples, resulting in a Li isotope
286 composition consistent with what is expected for the Al-Fe-associated Li pool.

287 Among these different Li pools, rinseable and carbonate Li have a minor effect
288 (<1.5% of total Li, Fig. S4) on the $\delta^7\text{Li}$ signatures of Ainsa sediments but the Al-Fe-
289 associated Li plays an important role on the bulk Li signature: sequential extractions
290 show that a significant portion (4% to 42% of bulk Li, Fig. S4) of light Li ($\delta^7\text{Li}=-6.0\text{‰}$
291 to -2.8‰) is present as an (Al-Fe)-associated Li pool in seawater-contacted (marine
292 and coastal) sediments, whereas this portion of Li is relatively smaller (5% to 16% of
293 bulk Li) and heavier ($\delta^7\text{Li}=-2.3\text{‰}$ to 0.1‰) in alluvial sediments. Although the
294 enrichment of ^6Li in the Al-Fe component is observed for both seawater-contacted and
295 alluvial sediments, the $\delta^7\text{Li}$ difference between this Li pool and bulk Li is generally

296 greater in the marine deposits than in the alluvial ones (Fig. S5).

297 **4. Discussion**

298 Overall, our results show that Li (and to a lesser extent Si) isotopes are very
299 sensitive proxies distinguishing between marine and continental depositional
300 environments – much more than concentrations of Li or other major/trace elements.
301 River studies have shown that one major cause of $\delta^7\text{Li}$ and $\delta^{30}\text{Si}$ variability in modern-
302 day river sediments is grain size (Bayon et al., 2018; Dellinger et al., 2014). In this
303 study, grain size effects were taken into account by comparing the isotopic signature of
304 different sedimentary bodies as a function of Al/Si. As indicated by Fig. 3, isotopic
305 shifts between alluvial and marine samples occur for all range of Al/Si values and are
306 therefore not due to changes in grain size. In the following, we thus discuss the possible
307 causes for the isotopic variabilities in Si and Li that characterize the Ainsa palaeo-delta
308 sediments.

309 **4.1 Ruling out the effect of temporal variations of rock source material and** 310 **weathering regime**

311 As pointed out above, the Ainsa palaeo-delta was formed within a couple of
312 million years. Because it was impossible to sample rocks of exactly the same age in the
313 field, a possible explanation of the variations in $\delta^7\text{Li}$ and $\delta^{30}\text{Si}$ of the different
314 sedimentary units could be temporal changes in the parent material or in the weathering
315 processes in the upstream watersheds.

316 As shown by a large number of studies, continental silicate rocks are rather
317 homogeneous in terms of $\delta^7\text{Li}$ and $\delta^{30}\text{Si}$, with the exception of shales, which are
318 enriched in Li and have lower $\delta^7\text{Li}$ and $\delta^{30}\text{Si}$ than granitic rocks (Dellinger et al., 2014;
319 Savage et al., 2013). If the Li isotopic variations reported in this study were essentially

320 due to mixing between different rock sources, Fig. 4 should be seen as a mixing diagram
321 between at least three end-members whose contribution changed with time. The
322 continental samples define a potential mixing line between a granitic end-member and
323 a shale end-member, close (but not exactly same) to what Dellinger et al. (2014) found
324 in the modern sediments transported by the Amazon and Mackenzie rivers ($\delta^7\text{Li}$
325 $=5\pm 1\%$, $\text{Li}/\text{Al} = 0.5\pm 0.1\times 10^{-3}$ for the granitic end-member and $\delta^7\text{Li} = 1\pm 1\%$, $\text{Li}/\text{Al} =$
326 $1\pm 0.1\times 10^{-3}$ for the shale end-member). However, the marine and coastal samples would
327 necessitate a third endmember, enriched in Li and more depleted in ^7Li , to be explained
328 (Fig. 4). Such an end-member has not been found in modern-day weathering products.
329 The fact that palaeogeographic reconstructions indicate no changes of provenance
330 during the construction of the Ainsa delta (Caja et al., 2010; Dreyer et al., 1999), and
331 that the Nd isotopes (not fractionated by weathering processes, McLennan, 1989) show
332 invariant ϵNd values (Fig. 3), also suggest a negligible variation of source rocks of all
333 samples measured in this study, which does not support the idea that the Li and Si
334 isotopic variability can be explained by a mixture of different parent materials changing
335 through time.

336 Alternatively, the observed isotopic changes between the different sediment
337 formations of the Ainsa palaeo-delta could be due to temporal variations in weathering
338 regimes within the sampled time window. We know from modern river systems that Li
339 isotope ratios of secondary solid products of chemical weathering vary as a function of
340 the weathering regime (Dellinger et al., 2017). Intensive weathering, *i.e.* high $W/(W+E)$
341 ratio (where W is the chemical erosion flux and E the physical erosion, Bouchez and
342 Gaillardet, 2014), results in lower river sediment $\delta^7\text{Li}$. Using this principle, the
343 difference in $\delta^7\text{Li}$ between marine and alluvial sediments could be interpreted as
344 resulting from different weathering regimes on the continent: a higher weathering

345 intensity reflected in the marine sediments compared to the alluvial ones. This scenario
346 would however imply a stronger Li-depletion in marine sediments, *i.e.* a stronger
347 solubilization of Li which produces lower Li/Al ratios in the solids (Dellinger et al.,
348 2014). We observe the opposite in Ainsa sediments (Fig. 4). Therefore, the observed
349 isotopic shifts between marine and alluvial sediments in Ainsa are unlikely to be related
350 to changes in provenance or weathering regime with time, but rather to processes that
351 operated in the palaeo-delta such as the scavenging of dissolved Li into sediments
352 through authigenic mineral formations.

353 **4.2 Evidence for the presence of an authigenic phase incorporating light Li and Si.**

354 We can interpret Fig. 4 as reflecting the existence of an authigenic component
355 contained in the marine sediments (and coastal sediments to a lesser extent), enriched
356 in Li (high Li/Al) and with $\delta^7\text{Li}$ lower than -3‰. Such a low value agrees with that
357 found in the leached phase in the HCl experiments.

358 The MQ rinsing experiments and the sequential extraction experiments using
359 HCl show that the only significant pool of extractable Li is associated with Al and Fe,
360 thus probably to Fe-bearing clay minerals, and that this Li pool displays a low $\delta^7\text{Li}$. The
361 absence of this Li fraction in the MQ rinsing solution suggests that this extractable Li
362 pool does not correspond to Li adsorbed or Li hosted in seawater inclusions. It is
363 important to note that all sediments groups from alluvial plains, coastal, and marine
364 environments show this extractable Li component even if it appears to be more
365 important in the seawater-contacted sediments. We interpret these results as indicating
366 the presence of an authigenic phase characterized by high contents of Al and Fe, mostly
367 present in the marine sediments of the Ainsa palaeo-delta. We emphasize that this Li
368 pool is a key to interrogate reverse weathering processes and it was often overlooked
369 in previous studies based on Li isotopes in sedimentary records (*e.g.* Yang et al., 2021).

370 From an isotopic point of view, it is now well admitted that the incorporation of
371 Li in secondary phases at low temperature favours the light Li isotope (*e.g.* Andrews et
372 al., 2020; Hindshaw et al., 2019; Vigier et al., 2008; Zhang et al., 2021). Leached
373 solutions from Ainsa sediments are enriched in ^6Li , and are therefore consistent with
374 the presence of an authigenic component. Authigenic clay formation has been
375 suggested to take place in the water column of an Icelandic estuary by Pogge von
376 Strandmann et al., (2008). In this study, the authors interpreted the $\delta^7\text{Li}$ of suspended
377 sediments as indicating the addition to basalt-derived detrital material of an authigenic
378 component having a $\delta^7\text{Li}$ 19‰ lower than seawater, consistent to the fractionation
379 factor ($\sim -20\%$) obtained from experimental studies (*e.g.* Zhang et al., 2021). Based on
380 the available seawater $\delta^7\text{Li}$ reconstructions, Eocene seawater $\delta^7\text{Li}$ should be close to
381 $\sim 24\%$ (Misra and Froelich, 2012) and thus inferred $\delta^7\text{Li}$ value of the Ainsa authigenic
382 component should be close to 4-5‰ assuming the same apparent fractionation factor.
383 This value is higher than the inferred authigenic component in this study ($< -3\%$),
384 suggesting that the authigenic phase in Ainsa may not have precipitated directly from
385 Eocene seawater. To explain the $< -3\%$ $\delta^7\text{Li}$ signature inferred from Fig. 4, applying a
386 Li isotope fractionation factor of $\sim -20\%$, the source of Li to authigenic phases should
387 have a $\delta^7\text{Li}$ signature lower than 17‰. A viable candidate for such a signature would
388 be the sediment porewater. Although it is impossible to know the local $\delta^7\text{Li}$ of the
389 porewater when Ainsa sedimentary rocks formed, we note that the modern pore water
390 recovered from coastal environments typically has $\delta^7\text{Li}$ values lower than that of
391 seawater (James and Palmer, 2000).

392 The effect of reverse weathering on oceanic Si isotope composition has been
393 long speculated (Frings et al., 2016 and references therein), and yet only limited
394 information is available from a handful of previous studies, which in particular showed

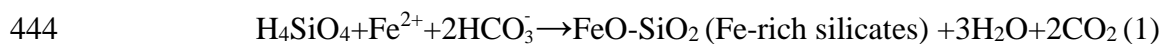
395 that authigenic clay formation is linked to the diagenesis of biogenic Si (BSi; *e.g.* Ehlert
396 et al., 2016; Geilert et al., 2020; Michalopoulos and Aller, 2004; Rahman et al., 2017,
397 2016). The Si isotope signature of the BSi source at Ainsa is unknown, which in
398 conjunction with the lack on constraints on Si isotope fractionation during BSi
399 diagenesis, hampers interpretation of our results beyond a first-order glimpse on the
400 potential role of authigenic clay formation on Si isotopes. However, the slight
401 difference in $\delta^{30}\text{Si}$ between the alluvial and seawater-contacted samples suggests that
402 the newly formed authigenic phase preferentially takes up light Si, in agreement with
403 previous findings from the precipitation of Si-bearing phases (*e.g.* Ehlert et al., 2016;
404 Geilert et al., 2020; Oelze et al., 2015).

405 Importantly, the lower $\delta^{30}\text{Si}$ signature of seawater-contacted sediments is
406 observed for samples with a high Al/Si ratio. In the context of previous studies on river
407 sediments (*e.g.* Bouchez et al., 2011), this can be interpreted as the fine end-member of
408 detrital sediment grain size undergoing the largest extent of authigenic clay formation,
409 provided that this latter reaction does not shift significantly the sediment Al/Si ratio
410 towards lower values through the incorporation of BSi. We argue that the Al/Si ratio is
411 relatively stable during these reactions. First, Al is an immobile element and the source
412 of Al for authigenic clay formation is thought to be the alteration of terrigenous Al-
413 oxides and aluminosilicates (Michalopoulos and Aller, 1995). Therefore, the bulk Al
414 content should be the same between continental and marine sediments. Regarding Si,
415 although we are still lacking detailed information on authigenic clay formation, this Si
416 flux to the sediment due to reverse weathering process is considered to be relatively
417 small (Frings et al., 2016) when compare to detrital Si content delivery to the oceans
418 (Milliman and Farnsworth, 2013). As both bulk sediment Al and Si concentrations are
419 not significantly modified by authigenic clay formation, the Al/Si ratio remains

420 relatively unchanged during diagenesis. As a consequence, the lower $\delta^{30}\text{Si}$ in high-Al/Si
421 marine sediments is indeed evidence for finer detrital fractions being more prone to
422 authigenic clay formation.

423 **4.3 A possible reverse weathering pathway coupling Fe cycle in marine** 424 **environment**

425 In the Ainsa palaeo-delta, the presence of authigenic clays is suggested by the
426 enrichment of light Li isotopes in seawater-contacted sediments. Moreover, the Li
427 isotope geochemistry is closely linked to Fe cycling in marine environments. First, as
428 indicated by Fig. 5, in bulk samples correlations exist between $\delta^7\text{Li}$ and Li/Fe or
429 Li/(Fe+Al), particularly for marine sediments. Second, the leaching experiment shows
430 that light Li isotopes, which is indicative of the authigenic clays, is associated with an
431 Al-Fe phase (Figs. S4 and S5). It is important to note that the range of isotopic values
432 found in this Al-Fe-associated Li pool is compatible with that inferred ($< -3\text{‰}$) from
433 the mixing diagram of Figs. 3 and 4. Beyond our study in Ainsa, the association
434 between $\delta^7\text{Li}$ and Fe content was also found in other marine sedimentary rocks (Qiu et
435 al., 2009). Therefore, our study provides evidence that reverse weathering, in certain
436 geological context such as deltas, is coupled with the marine Fe cycle. Indeed, river
437 deltas are known to act as a major sink of riverine dissolved Fe through colloidal
438 flocculation and particle adsorption (*e.g.* Sholkovitz, 1976). The rapid formation of
439 Fe-bearing products could then lead to efficient light Li sorption in the water column
440 (Pistiner and Henderson, 2003). Once deposited in the sediment column, early
441 diagenesis in reducing marine environments would then allow for the formation of
442 Fe^{2+} -rich phases, such as oxides and Fe-rich aluminosilicates. Such processes can be
443 possibly achieved by following reaction:



445 The Fe-rich silicates minerals could incorporate Li, as Li^+ and Fe^{2+} share similar ionic
446 radii (Shannon, 1976). Iron-rich compositions are a common feature of authigenic
447 minerals such as greenalite and odinite (*e.g.* Isson and Planavsky, 2018), which form
448 relatively rapidly in the sediment column (Michalopoulos and Aller, 2004, 1995). This
449 Fe-rich phase is likely driven by the co-precipitation of Fe and Si (*e.g.* Wu et al., 2012).
450 The association of Li with an Al–Fe pool in Ainsa sediments can therefore be
451 interpreted as the formation of authigenic clays in a reducing environment in the delta,
452 for example in the sedimentary column.

453 A recent study of the authigenic formation effect on Li geochemistry in a
454 carbonate-rich unit from deep-sea environment (Andrews et al., 2020) suggests that
455 significant clay neof ormation occurs in the sedimentary column at depth further away
456 from the seawater-sediment interface. In contrast to results from an estuary in Iceland
457 (Pogge von Strandmann et al., 2008) and experimental constraints on authigenic
458 formation (Zhang et al., 2021), where rapid early diagenesis predominate, slow burial
459 diagenesis controls the uptake of Li into authigenic phase at geological time scales.
460 Although our limited dataset does not permit us to fully explore the roles of both early
461 and burial diagenesis, we speculate that our results are driven by early diagenesis
462 processes as the authigenic phase is closely coupled to rapid Fe cycle (*e.g.* Sholkovitz,
463 1976) and the deltaic environments, where detrital materials are abundant and these
464 materials can be further dissolved during the interaction with seawater, allows for early
465 diagenesis processes (*e.g.* Michalopoulos and Aller, 1995). Furthermore, the $\delta^7\text{Li}$
466 fingerprint used in this study to trace authigenic formation shows a gradual decrease
467 along the land-to-sea continuum, and the authigenic phase is not only observed in
468 marine sediments but also in coastal settings where the burial effect is minor. This
469 suggests the authigenic processes occurred in the Ainsa delta was rather impacted by

470 early diagenesis effects.

471 At the Ainsa palaeo-delta, we observe that these reactions tied to Fe act as a sink
472 for Li into the sediments and causes a fractionation resulting in a heavier $\delta^7\text{Li}$ in water.
473 This deltaic process identified in this study therefore contributes to enrich marine shales
474 in Li (Dellinger et al., 2014) even if the Li/Al difference between marine and non-
475 marine material is tight (Fig. 4). The contradictory observation between Ainsa marine
476 sediments where light Li is preferred and shales having heavy $\delta^7\text{Li}$ values (Teng et al.,
477 2004) indicates other mechanisms enriching Li in marine sedimentary rocks, such as
478 the precipitation of other Li-bearing phases in other geological contexts or more
479 probably during burial diagenesis (Andrews et al., 2020). The enrichment of Na in the
480 seawater-contacted sediments observed at Ainsa compared to alluvial sediments (Fig.
481 5) is noteworthy. As the Na abundance of the HCl-leach extracts is similar among
482 different environments, the enrichment of Na in the coastal and marine sediments can
483 be attributed to its incorporation into authigenic phases (*e.g.* phyllosilicates), rather than
484 to seawater inclusions. Nevertheless, the enrichment of the heavy alkali elements K,
485 Rb, and Cs is less significant in the case of Ainsa (Table S5). Although K has been
486 shown to be taken up by reverse weathering reactions (*e.g.* Michalopoulos and Aller,
487 1995), our results suggest the diagenetic phases that formed in the Ainsa delta do not
488 play a major role of seawater K sequestration. This difference in terms of K uptake
489 between a palaeo-delta archive (this study) and modern delta systems (Michalopoulos
490 and Aller, 1995) requires further work to understand the mechanism controlling K sinks
491 in the ocean (Holland, 2005).

492 **5. Conclusion**

493 The fact that at Ainsa, the Si and Li isotope compositions in marine and coastal

494 plain sediments are lighter than in alluvial ones, together with the associated enrichment
495 in the soluble cation Li and Na, suggest that formation of Fe-rich authigenic clays in
496 deltaic environments is an important process for ocean elemental and isotope budgets.

497 Our results show that light Li is incorporated into seawater-contacted sediments,
498 particularly the marine sediments in deltaic environments, resulting in a lower $\delta^7\text{Li}$
499 signature than in alluvial ones. This observation is in contrast to that made on ancient,
500 fine-grained marine sedimentary rocks (Dellinger et al., 2014; Teng et al., 2004).
501 Similar to continental weathering processes which can not be ascribed to a single
502 reaction, reverse weathering reactions are likely associated with complex diagenesis
503 processes and different yet-unidentified reactions, and here we have one which couples
504 Li, Si, and Fe cycles in the deltas.

505 Furthermore, our study supports a strong coupling among Fe, Li, and Si in deltaic
506 environments (coastal and marine) through the neof ormation of authigenic
507 phyllosilicates in reducing conditions. This process is typical of a reverse weathering
508 reaction as proposed initially, in that it consumes alkalinity and produces CO_2 in the
509 atmosphere-ocean system (Isson et al., 2020; Mackenzie and Garrels, 1966; Sillen,
510 1967). By consuming ocean alkalinity, it acts as a counterbalancing reaction to the
511 neutralization of atmospheric CO_2 through silicate weathering reactions transforming
512 rocks into soils in the terrestrial Critical Zone. Finally, our investigation clearly
513 demonstrates that reverse weathering reactions existed at the time of deposition, and Li
514 isotopes can be useful to constrain the marine or continental origin of sedimentary rocks.
515 Such a tool is important in paleo-environmental studies including reconstruction of past
516 living environments or the formation of mountain ranges when arguments based on
517 sedimentary facies or fossil organisms are not conclusive.

518

519 **Acknowledgements**

520 We sincerely thank those helped in this project, particularly Amandine Laborde for
521 sampling assistance in the field, Marc Quintin for thin section preparation, and Laëticia
522 Faure for Nd isotope analysis. This research is fully funded by the People Programme
523 (Marie Curie Actions) of the European Union's Seventh Framework Programme
524 FP7/2007-2013/ under REA grant agreement [608069, ISONOSE]. Part of this work
525 was supported by the IPGP multidisciplinary program PARI and the Region île-de-
526 France SESAME Grant no. 12015908.

527 **References:**

- 528 Andrews, E., Pogge von Strandmann, P.A.E., Fantle, M.S., 2020. Exploring the
529 importance of authigenic clay formation in the global Li cycle. *Geochim.*
530 *Cosmochim. Acta* 289, 47–68. <https://doi.org/10.1016/j.gca.2020.08.018>
- 531 Bastian, L., Vigier, N., Reynaud, S., Kerros, M.-E., Revel, M., Bayon, G., 2018.
532 Lithium Isotope Composition of Marine Biogenic Carbonates and Related
533 Reference Materials. *Geostand. Geoanalytical Res.* 42, 403–415.
534 <https://doi.org/10.1111/ggr.12218>
- 535 Bayon, G., Delvigne, C., Ponzevera, E., Borges, A. V, Darchambeau, F., De Deckker,
536 P., Lambert, T., Monin, L., Toucanne, S., André, L., 2018. The silicon isotopic
537 composition of fine-grained river sediments and its relation to climate and
538 lithology. *Geochim. Cosmochim. Acta* 229, 147–161.
- 539 Bernhardt, A., Oelze, M., Bouchez, J., von Blanckenburg, F., Mohtadi, M., Christl, M.,
540 Wittmann, H., 2020. $^{10}\text{Be}/^{9}\text{Be}$ ratios reveal marine authigenic clay formation.
541 *Geophys. Res. Lett.* 47, e2019GL086061. <https://doi.org/10.1029/2019GL086061>
- 542 Bhattacharya, J.P.P., 2006. *Deltas, Facies Models Revisited*. SEPM Society for
543 *Sedimentary Geology*. <https://doi.org/10.2110/pec.06.84.0237>
- 544 Bouchez, J., Gaillardet, J., 2014. How accurate are rivers as gauges of chemical
545 denudation of the Earth surface? *Geology* 42, 171–174.
- 546 Bouchez, J., Lupker, M., Gaillardet, J., France-Lanord, C., Maurice, L., 2011a. How
547 important is it to integrate riverine suspended sediment chemical composition with
548 depth? Clues from Amazon River depth-profiles. *Geochim. Cosmochim. Acta* 75,
549 6955–6970. <https://doi.org/https://doi.org/10.1016/j.gca.2011.08.038>
- 550 Bouchez, J., Métivier, F., Lupker, M., Maurice, L., Perez, M., Gaillardet, J., France-
551 Lanord, C., 2011b. Prediction of depth-integrated fluxes of suspended sediment in

552 the Amazon River: particle aggregation as a complicating factor. *Hydrol. Process.*
553 25, 778–794. <https://doi.org/10.1002/hyp.7868>

554 Caja, M.A., Marfil, R., Garcia, D., Remacha, E., Morad, S., Mansurbeg, H., Amorosi,
555 A., Martínez-Calvo, C., Lahoz-Beltrá, R., 2010. Provenance of siliciclastic and
556 hybrid turbiditic arenites of the Eocene Hecho Group, Spanish Pyrenees:
557 implications for the tectonic evolution of a foreland basin. *Basin Res.* 22, 157–180.
558 <https://doi.org/10.1111/j.1365-2117.2009.00405.x>

559 Dellinger, M., Bouchez, J., Gaillardet, J., Faure, L., Moureau, J., 2017. Tracing
560 weathering regimes using the lithium isotope composition of detrital sediments.
561 *Geology* 45, 411–414.

562 Dellinger, M., Gaillardet, J., Bouchez, J., Calmels, D., Galy, V., Hilton, R.G., Louvat,
563 P., France-Lanord, C., 2014. Lithium isotopes in large rivers reveal the
564 cannibalistic nature of modern continental weathering and erosion. *Earth Planet.*
565 *Sci. Lett.* 401, 359–372.
566 <https://doi.org/http://dx.doi.org/10.1016/j.epsl.2014.05.061>

567 Dreyer, T., Corregidor, J., Arbues, P., Puigdefabregas, C., 1999. Architecture of the
568 tectonically influenced Sobrarbe deltaic complex in the Ainsa Basin, northern
569 Spain. *Sediment. Geol.* 127, 127–169.

570 Ehlert, C., Doering, K., Wallmann, K., Scholz, F., Sommer, S., Grasse, P., Geilert, S.,
571 Frank, M., 2016. Stable silicon isotope signatures of marine pore waters –
572 Biogenic opal dissolution versus authigenic clay mineral formation. *Geochim.*
573 *Cosmochim. Acta* 191, 102–117.
574 <https://doi.org/https://doi.org/10.1016/j.gca.2016.07.022>

575 Fedo, C.M., Wayne Nesbitt, H., Young, G.M., 1995. Unraveling the effects of
576 potassium metasomatism in sedimentary rocks and paleosols, with implications

577 for paleoweathering conditions and provenance. *Geology* 23, 921–924.
578 [https://doi.org/10.1130/0091-7613\(1995\)023<0921:UTEOPM>2.3.CO;2](https://doi.org/10.1130/0091-7613(1995)023<0921:UTEOPM>2.3.CO;2)

579 Frings, P.J., Clymans, W., Fontorbe, G., De La Rocha, C.L., Conley, D.J., 2016. The
580 continental Si cycle and its impact on the ocean Si isotope budget. *Chem. Geol.*
581 425, 12–36. <https://doi.org/http://dx.doi.org/10.1016/j.chemgeo.2016.01.020>

582 Geilert, S., Grasse, P., Doering, K., Wallmann, K., Ehlert, C., Scholz, F., Frank, M.,
583 Schmidt, M., Hensen, C., 2020. Impact of ambient conditions on the Si isotope
584 fractionation in marine pore fluids during early diagenesis. *Biogeosciences* 17,
585 1745–1763. <https://doi.org/10.5194/bg-17-1745-2020>

586 Golla, J.K., Kuessner, M.L., Henehan, M.J., Bouchez, J., Rempe, D.M., Druhan, J.L.,
587 2021. The evolution of lithium isotope signatures in fluids draining actively
588 weathering hillslopes. *Earth Planet. Sci. Lett.* 567, 116988.
589 <https://doi.org/https://doi.org/10.1016/j.epsl.2021.116988>

590 Hindshaw, R.S., Tosca, R., Goût, T.L., Farnan, I., Tosca, N.J., Tipper, E.T., 2019.
591 Experimental constraints on Li isotope fractionation during clay formation.
592 *Geochim. Cosmochim. Acta* 250, 219–237.

593 Holland, H.D., 2005. Sea level, sediments and the composition of seawater. *Am. J. Sci.*
594 305, 220–239.

595 Huh, Y., Chan, L.-H., Zhang, L., Edmond, J.M., 1998. Lithium and its isotopes in major
596 world rivers: implications for weathering and the oceanic budget. *Geochim.*
597 *Cosmochim. Acta* 62, 2039–2051. [https://doi.org/https://doi.org/10.1016/S0016-](https://doi.org/https://doi.org/10.1016/S0016-7037(98)00126-4)
598 [7037\(98\)00126-4](https://doi.org/https://doi.org/10.1016/S0016-7037(98)00126-4)

599 Isson, T.T., Planavsky, N.J., 2018. Reverse weathering as a long-term stabilizer of
600 marine pH and planetary climate. *Nature* 560, 471.

601 Isson, T.T., Planavsky, N.J., Coogan, L.A., Stewart, E.M., Ague, J.J., Bolton, E.W.,

602 Zhang, S., McKenzie, N.R., Kump, L.R., 2020. Evolution of the Global Carbon
603 Cycle and Climate Regulation on Earth. *Global Biogeochem. Cycles* 34,
604 e2018GB006061. [https://doi.org/https://doi.org/10.1029/2018GB006061](https://doi.org/10.1029/2018GB006061)

605 James, R.H., Palmer, M.R., 2000. Marine geochemical cycles of the alkali elements and
606 boron: the role of sediments. *Geochim. Cosmochim. Acta* 64, 3111–3122.
607 [https://doi.org/https://doi.org/10.1016/S0016-7037\(00\)00418-X](https://doi.org/10.1016/S0016-7037(00)00418-X)

608 Li, G., West, A.J., 2014. Evolution of Cenozoic seawater lithium isotopes: Coupling of
609 global denudation regime and shifting seawater sinks. *Earth Planet. Sci. Lett.* 401,
610 284–293.

611 Mackenzie, F.T., Garrels, R.M., 1966. Chemical mass balance between rivers and
612 oceans. *Am. J. Sci.* 264, 507–525.

613 McLennan, S.M., 1989. Rare earth elements in sedimentary rocks; influence of
614 provenance and sedimentary processes. *Rev. Mineral. Geochemistry* 21, 169–200.

615 Michalopoulos, P., Aller, R.C., 2004. Early diagenesis of biogenic silica in the Amazon
616 delta: alteration, authigenic clay formation, and storage. *Geochim. Cosmochim.*
617 *Acta* 68, 1061–1085.

618 Michalopoulos, P., Aller, R.C., 1995. Rapid Clay Mineral Formation in Amazon Delta
619 Sediments: Reverse Weathering and Oceanic Elemental Cycles. *Science* (80-.).
620 270, 614–617.

621 Milliman, J.D., Farnsworth, K.L., 2013. River discharge to the coastal ocean: a global
622 synthesis. Cambridge University Press.

623 Misra, S., Froelich, P.N., 2012. Lithium Isotope History of Cenozoic Seawater:
624 Changes in Silicate Weathering and Reverse Weathering. *Science* (80-.). 335,
625 818–823. <https://doi.org/10.1126/science.1214697>

626 Nägler, T.F., Schafer, H.-J., Gebauer, D., 1995. Evolution of the Western European

627 continental crust: implications from Nd and Pb isotopes in Iberian sediments.
628 Chem. Geol. 121, 345–357. <https://doi.org/https://doi.org/10.1016/0009->
629 2541(94)00129-V

630 Oelze, M., von Blanckenburg, F., Bouchez, J., Hoellen, D., Dietzel, M., 2015. The
631 effect of Al on Si isotope fractionation investigated by silica precipitation
632 experiments. Chem. Geol. <https://doi.org/http://dx.doi.org.insu.bib.cnrs.fr/10.1016/j.chemgeo.2015.01.002>

634 Pedregosa, F., Varoquaux, G., Gramfort, A., Michel, V., Thirion, B., Grisel, O., Blondel,
635 M., Prettenhofer, P., Weiss, R., Dubourg, V., Vanderplas, J., Passos, A.,
636 Cournapeau, D., Brucher, M., Perrot, M., Duchesnay, E., 2011. Scikit-learn:
637 Machine Learning in {P}ython. J. Mach. Learn. Res. 12, 2825–2830.

638 Pickering, K.T., Bayliss, N.J., 2009. Deconvolving tectono-climatic signals in deep-
639 marine siliciclastics, Eocene Ainsa basin, Spanish Pyrenees: Seesaw tectonics
640 versus eustasy. Geology 37, 203–206.

641 Pickering, K.T., Corregidor, J., 2005. Mass-Transport Complexes (MTCs) and
642 Tectonic Control on Basin-Floor Submarine Fans, Middle Eocene, South Spanish
643 Pyrenees. J. Sediment. Res. 75, 761–783. <https://doi.org/10.2110/jsr.2005.062>

644 Pistiner, J.S., Henderson, G.M., 2003. Lithium-isotope fractionation during continental
645 weathering processes. Earth Planet. Sci. Lett. 214, 327–339.

646 Pogge von Strandmann, P.A.E., James, R.H., van Calsteren, P., Gíslason, S.R., Burton,
647 K.W., 2008. Lithium, magnesium and uranium isotope behaviour in the estuarine
648 environment of basaltic islands. Earth Planet. Sci. Lett. 274, 462–471.

649 Qiu, L., Rudnick, R.L., McDonough, W.F., Merriman, R.J., 2009. Li and $\delta^7\text{Li}$ in
650 mudrocks from the British Caledonides: metamorphism and source influences.
651 Geochim. Cosmochim. Acta 73, 7325–7340.

652 Rahman, S., Aller, R.C., Cochran, J.K., 2017. The Missing Silica Sink: Revisiting the
653 Marine Sedimentary Si Cycle Using Cosmogenic ^{32}Si . *Global Biogeochem.*
654 *Cycles* 31, 1559–1578. <https://doi.org/10.1002/2017GB005746>

655 Rahman, S., Aller, R.C., Cochran, J.K., 2016. Cosmogenic ^{32}Si as a tracer of biogenic
656 silica burial and diagenesis: Major deltaic sinks in the silica cycle. *Geophys. Res.*
657 *Lett.* 43, 7124–7132.

658 Santiago Ramos, D.P., Coogan, L.A., Murphy, J.G., Higgins, J.A., 2020. Low-
659 temperature oceanic crust alteration and the isotopic budgets of potassium and
660 magnesium in seawater. *Earth Planet. Sci. Lett.* 541, 116290.
661 <https://doi.org/https://doi.org/10.1016/j.epsl.2020.116290>

662 Savage, P.S., Georg, R.B., Williams, H.M., Halliday, A.N., 2013. The silicon isotope
663 composition of the upper continental crust. *Geochim. Cosmochim. Acta* 109, 384–
664 399. <https://doi.org/http://dx.doi.org/10.1016/j.gca.2013.02.004>

665 Shannon, R.D., 1976. Revised effective ionic radii and systematic studies of interatomic
666 distances in halides and chalcogenides. *Acta Crystallogr. Sect. A Cryst. physics,*
667 *diffraction, Theor. Gen. Crystallogr.* 32, 751–767.
668 <https://doi.org/10.1107/S0567739476001551>

669 Sholkovitz, E.R., 1976. Flocculation of dissolved organic and inorganic matter during
670 the mixing of river water and seawater. *Geochim. Cosmochim. Acta* 40, 831–845.

671 Sillen, L.G., 1967. The ocean as a chemical system. *Science* 156, 1189–1197.
672 <https://doi.org/156/3779/1189> [pii]

673 Teng, F.-Z., McDonough, W.F., Rudnick, R.L., Dalpé, C., Tomascak, P.B., Chappell,
674 B.W., Gao, S., 2004. Lithium isotopic composition and concentration of the upper
675 continental crust. *Geochim. Cosmochim. Acta* 68, 4167–4178.

676 Vigier, N., Decarreau, A., Millot, R., Carignan, J., Petit, S., France-Lanord, C., 2008.

677 Quantifying Li isotope fractionation during smectite formation and implications
678 for the Li cycle. *Geochim. Cosmochim. Acta* 72, 780–792.

679 Wu, L., Percak-Dennett, E.M., Beard, B.L., Roden, E.E., Johnson, C.M., 2012. Stable
680 iron isotope fractionation between aqueous Fe(II) and model Archean ocean Fe–
681 Si coprecipitates and implications for iron isotope variations in the ancient rock
682 record. *Geochim. Cosmochim. Acta* 84, 14–28.
683 <https://doi.org/https://doi.org/10.1016/j.gca.2012.01.007>

684 Yang, C., Vigier, N., Yang, S., Revel, M., Bi, L., 2021. Clay Li and Nd isotopes
685 response to hydroclimate changes in the Changjiang (Yangtze) basin over the past
686 14,000 years. *Earth Planet. Sci. Lett.* 561, 116793.
687 <https://doi.org/https://doi.org/10.1016/j.epsl.2021.116793>

688 Zhang, X. (Yvon), Saldi, G.D., Schott, J., Bouchez, J., Kuessner, M., Montouillout, V.,
689 Henehan, M., Gaillardet, J., (Yvon) Zhang, X., Saldi, G.D., Schott, J., Bouchez, J.,
690 Kuessner, M., Montouillout, V., Henehan, M., Gaillardet, J., 2021. Experimental
691 constraints on Li isotope fractionation during the interaction between kaolinite and
692 seawater. *Geochim. Cosmochim. Acta* 292, 333–347.
693 <https://doi.org/https://doi.org/10.1016/j.gca.2020.09.029>

694

1 **Figure captions**

2 **Figure 1. Simplified (A) structural scheme of the southwestern Pyrenees Mountain**
3 **range, (B) geological map of the Ainsa Basin, and (C) longitudinal profile across**
4 **the palaeo-deltaic system of the Ainsa Basin (modified after Dreyer et al., (1999)).**
5 **Ja: Jabierre de Olsón, Es: Escanilla, Me: Mesón de Ligüerre, and Co: Coscojuela**
6 **sampling sites (see Fig. S1 for sedimentological sections).**

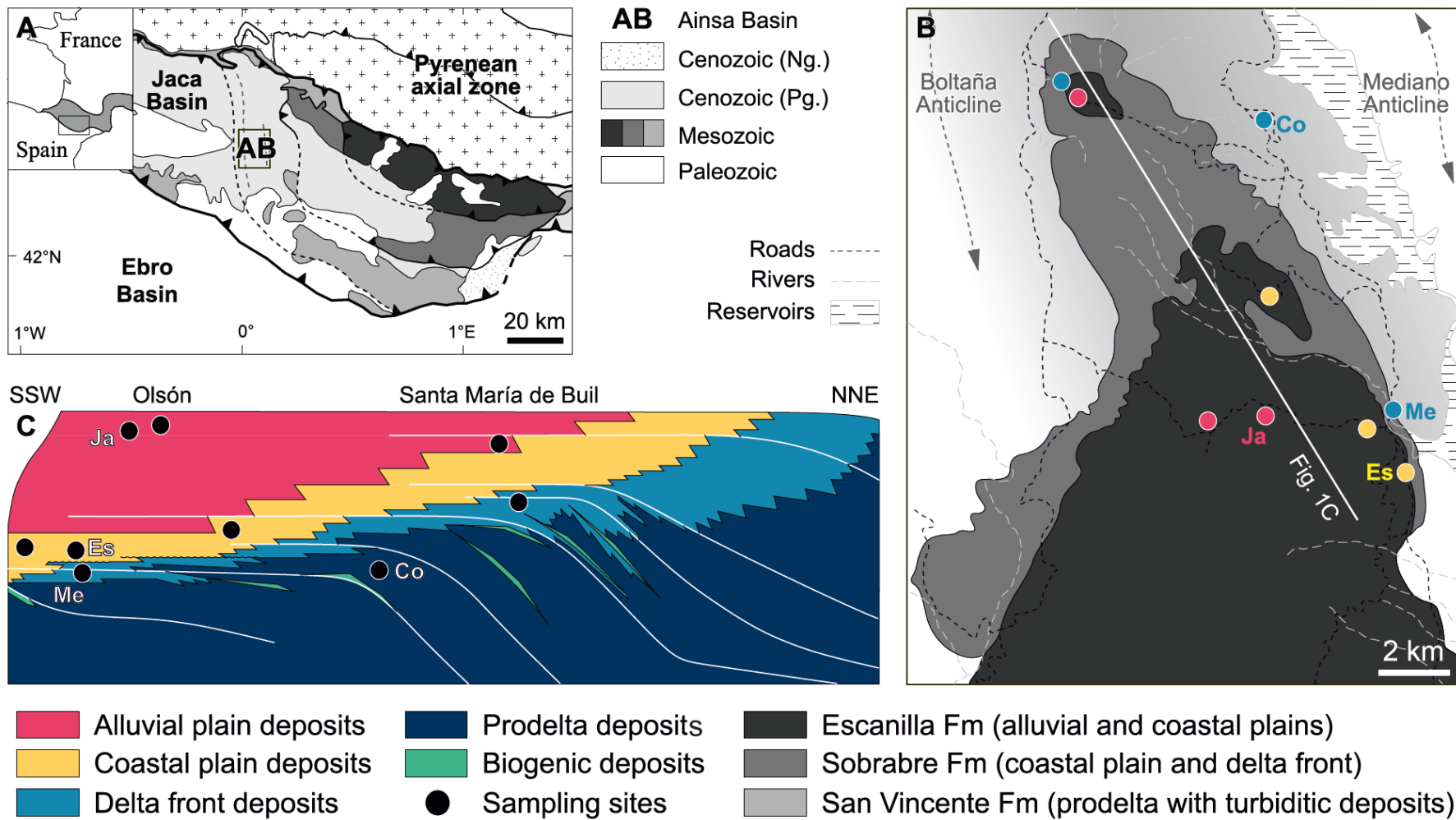
7 **Figure 2. “Box plots” of (A) major and (B) trace element concentrations**
8 **normalized to Al for sediments from different depositional environments of the**
9 **Ainsa Basin. Elements are ranked by increasing mean X/Al ratios from Mn to Ca**
10 **and from Cs to Sr. Only a limited number of elements show enrichments in the**
11 **seawater-contacted sediments compared to their terrestrial counterparts: Na and**
12 **Fe for the major elements, and Li for trace elements.**

13 **Figure 3. Grain size (indexed by the Al/Si ratio) distribution of lithium (top),**
14 **neodymium (middle), and silicon (bottom) isotope systems for bulk sediments of**
15 **the alluvial plain, coastal plain, and marine (delta front and prodelta) depositional**
16 **environments from the Ainsa Basin. Best-fit lines for relationships between isotope**
17 **signatures (Li and Si) and grain size are shown as short dashed lines.**

18 **Figure 4. Relationship between $\delta^7\text{Li}$ values and Li/Al ratios of the alluvial plain,**
19 **coastal plain, and marine (delta front and prodelta) depositional environments**
20 **from the Ainsa Basin. The grey bar shows the “baseline” formed by the**
21 **composition of sediments without marine influence, and the arrows indicate the**
22 **departure of sediments from this baseline towards Li enriched compositions and**
23 **lower $\delta^7\text{Li}$ values, due to authigenic clay formation in the marine realm. The**
24 **estimated probability densities of Li/Al and $\delta^7\text{Li}$ for each sediments group are**

25 respectively displayed at the top and the right of the figure. The most ^6Li -enriched
26 samples provide an upper boundary on the $\delta^7\text{Li}$ of the authigenic component,
27 which we estimate at -3‰.

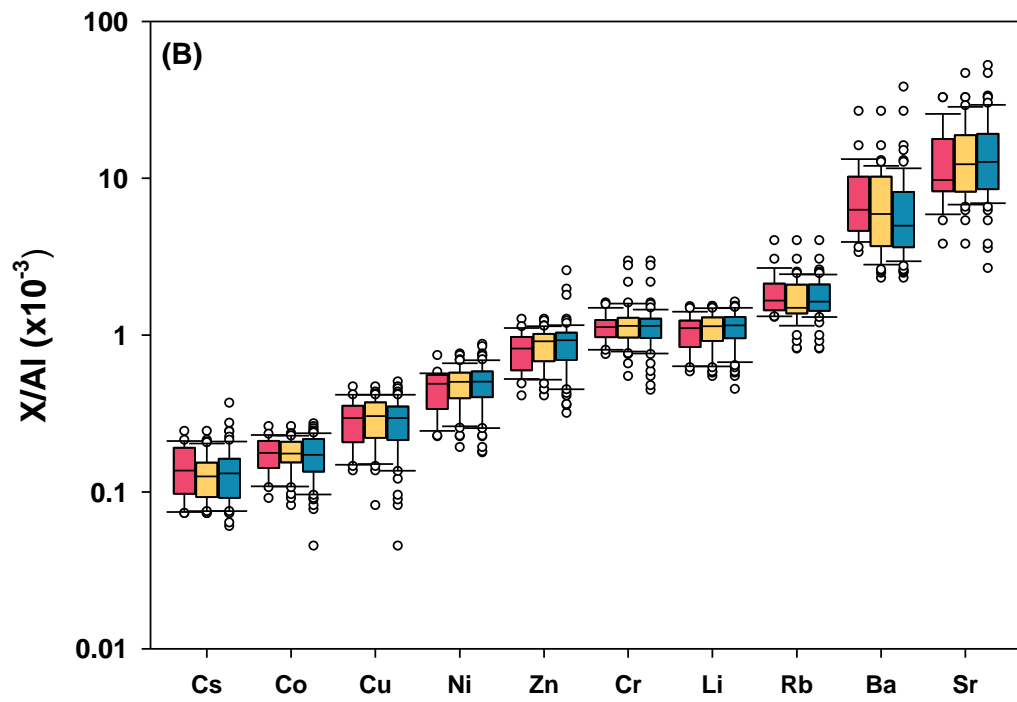
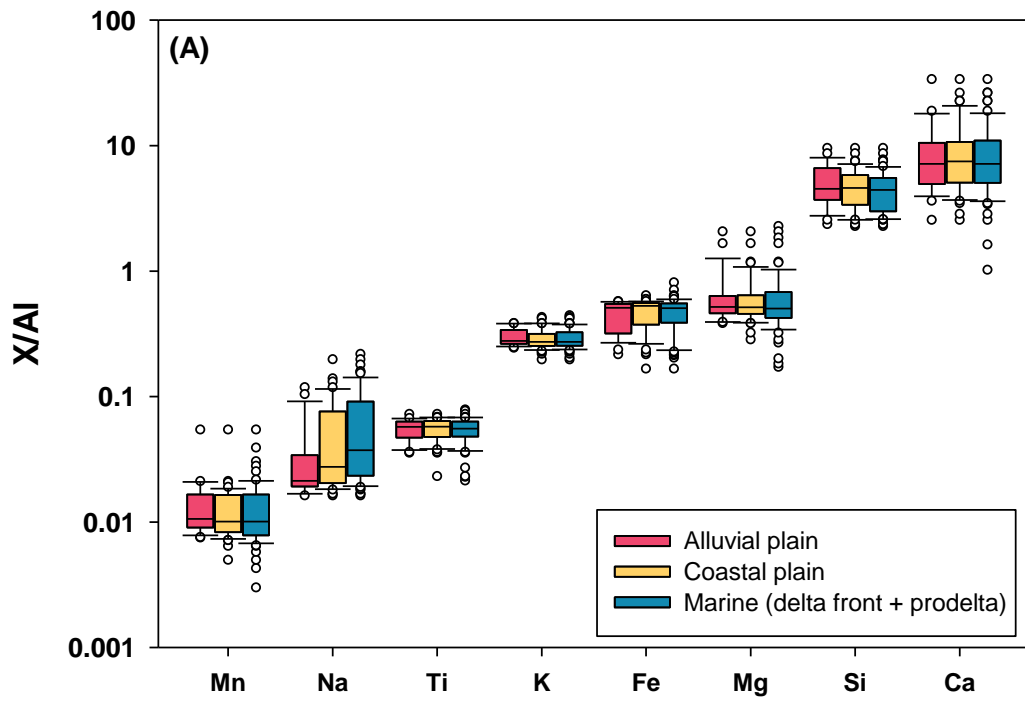
28 **Figure 5. Relationships between $\delta^7\text{Li}$ values and $\text{Li}/(\text{Al}+\text{Fe})$, $\text{Na}/(\text{Al}+\text{Fe})$ and**
29 **$\text{Li}/(\text{Al}+\text{Fe})$ ratios, and $\delta^7\text{Li}$ values and Li/Fe ratio in sediments of the alluvial plain,**
30 **coastal plain, and marine (delta front and prodelta) depositional environments**
31 **from the Ainsa Basin. Best-fit lines are shown as short dashed lines. Colors for**
32 **different samples are the same as in Fig. 1.**



33

34

Figure 1



35

36

37

38

Figure 2

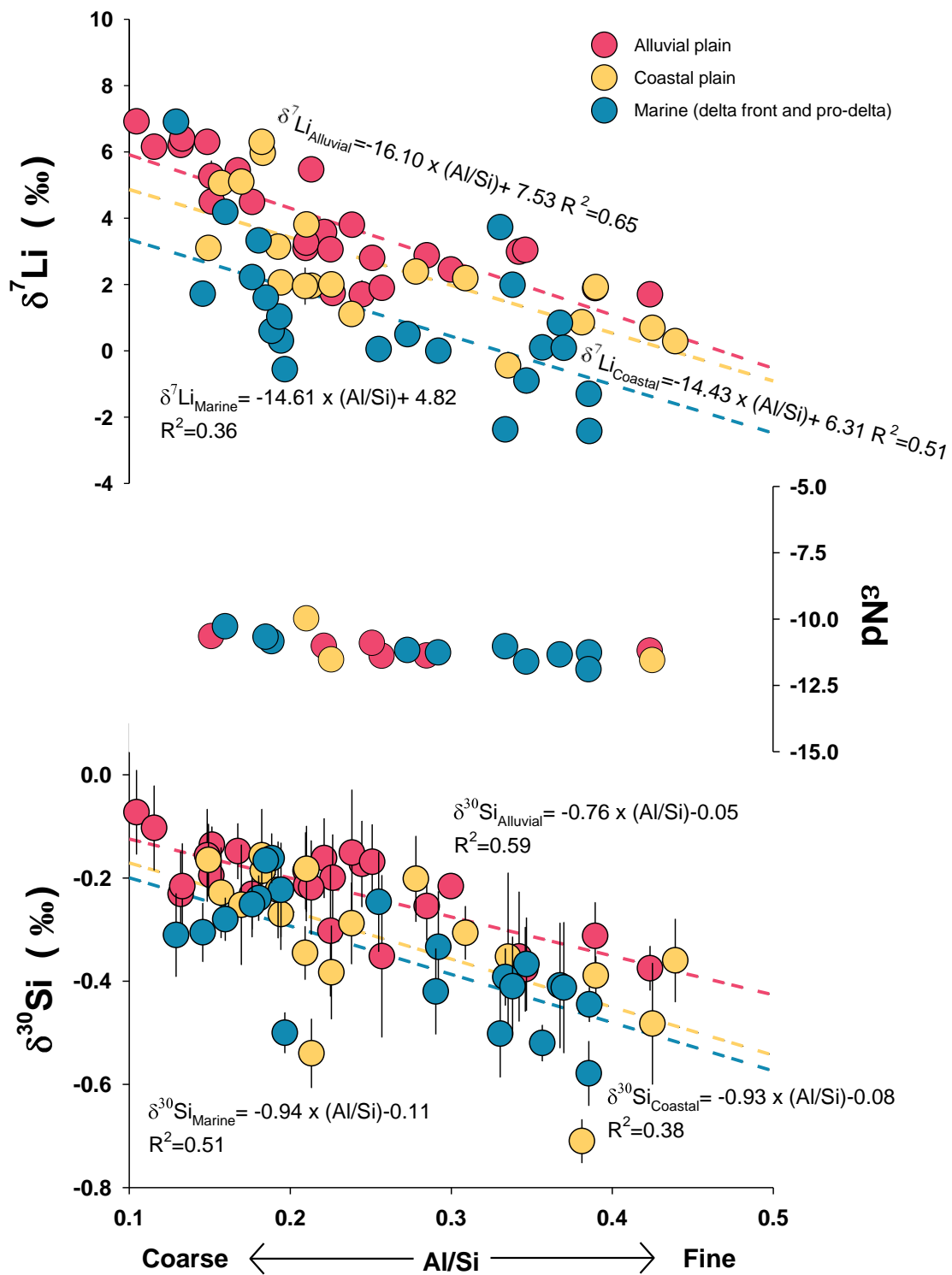


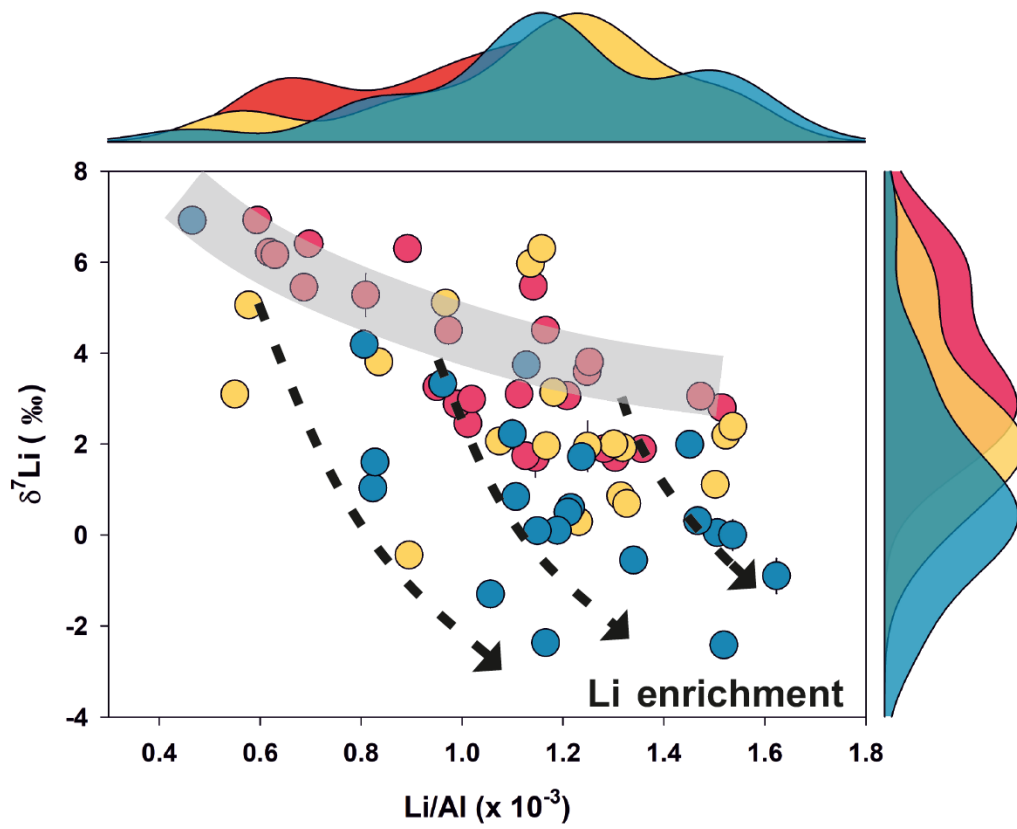
Figure 3

39

40

41

42

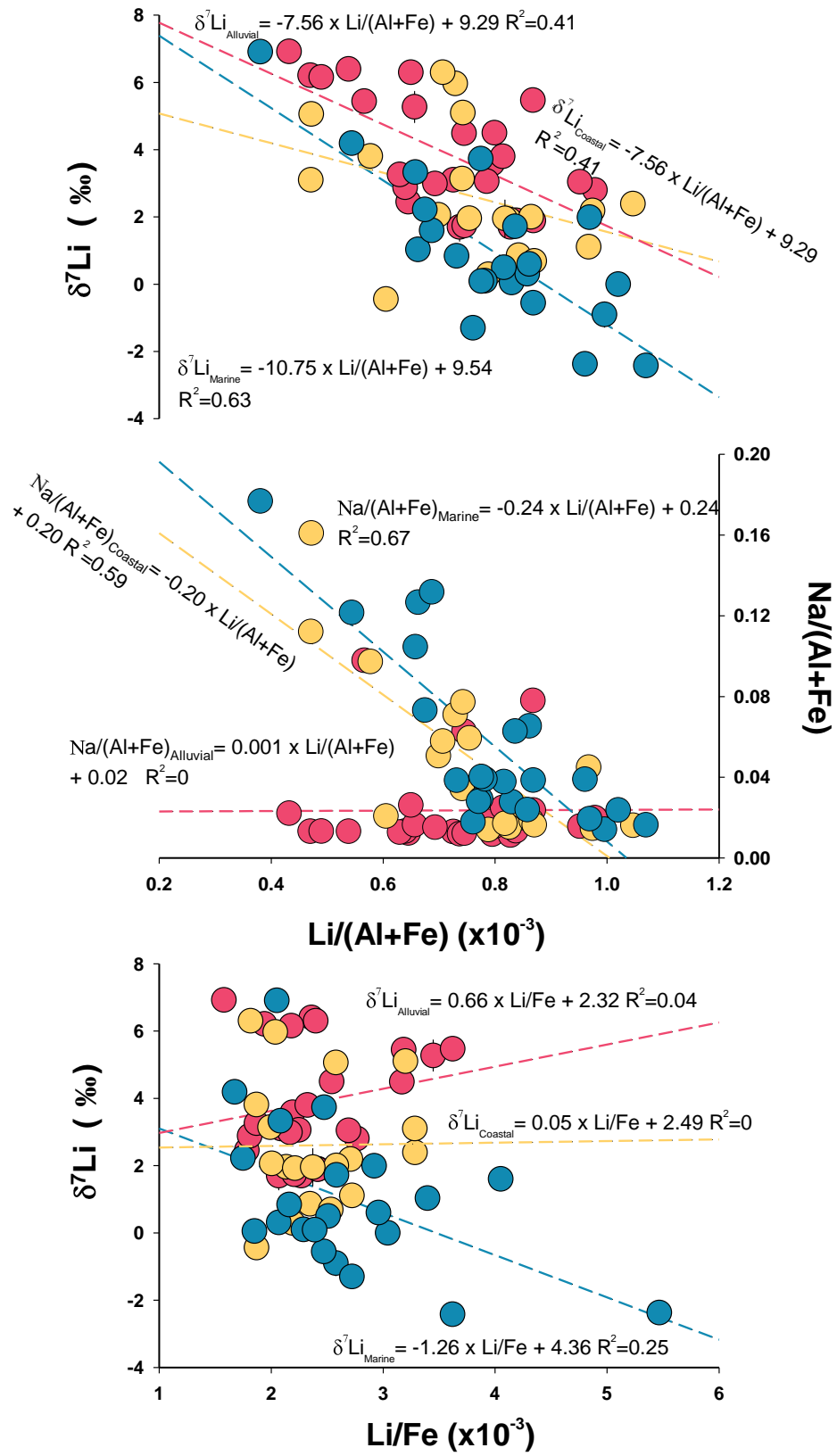


43

44

45

Figure 4



46

47

Figure 5

1 **Table captions**

2 **Table 1.** Summary of the thin section observations.

3 **Table 2.** Amount of Li extracted by the water rinsing experiments (in % of bulk
4 content).

5 **Table 3.** Li isotope composition of the first and the last leach solution obtained from
6 the HCl-leaching experiments.

7

8

9 **Supplementary tables**

10 **Table S1.** Locations, depositional environments, $\delta^7\text{Li}$ and $\delta^{30}\text{Si}$ values (in ‰), ϵNd ,
11 and Al/Si ratios of the samples collected in the Ainsa Basin.

12 **Table S2.** Major element concentrations (expressed in weight percent oxides) of the
13 samples collected in the Ainsa Basin.

14
15 **Table S3.** Trace elements concentrations (in ppm) of the samples collected in the Ainsa
16 Basin.

17
18 **Table S4.** HCl extracted cations (Ca, Li, Al, and Fe) in proportion to bulk sample (%).
19

20 **Table S5.** Average alkali elements concentration (normalized to Al) in sediments
21 deposited in different environments.

22

23

Table 1. Summary of the thin section observations.

<i>Depositional environment</i>	<i>Coarse fraction</i>	<i>Fine fraction</i>
Alluvial	Coarse- to medium-grained sandstones mainly composed of angular to subangular detrital quartz and carbonates (crystalline, bioclastic, and micritic limestones), together with common detrital oxides or hydroxides and a few unweathered grains of detrital feldspars, micas, pyroxene, amphiboles, sandstones, and siltstones, surrounded by a calcite cement <i>Example: sample SA 13 (Fig. S2A)</i>	Medium-grained sandstones to siltstones mainly composed of subangular detrital quartz and carbonates (crystalline and micritic limestones), together with common detrital oxides or hydroxides and a few unweathered grains of detrital feldspars, micas, pyroxene, amphiboles, and siltstones, surrounded by a clay matrix and/or a calcite cement <i>Example: sample SA 15 (Fig. S2B)</i>
Coastal	Coarse- to medium-grained sandstones mainly composed of angular to subangular detrital quartz and carbonates (crystalline, bioclastic, and micritic limestones), together with common detrital oxides or hydroxides and a few unweathered grains of detrital feldspars, micas, pyroxene, amphiboles, sandstones, and siltstones, surrounded by a calcite cement <i>Example: sample SC 6 (Fig. S2C)</i>	Medium-grained sandstones to siltstones mainly composed of subangular detrital quartz and carbonates (crystalline and micritic limestones), together with common detrital oxides or hydroxides and a few unweathered grains of detrital feldspars, micas, pyroxene, amphiboles, and siltstones, surrounded by a clay matrix and/or a calcite cement <i>Example: sample SC 8 (Fig. S2D)</i>
Marine	Coarse- to medium-grained sandstones mainly composed of angular to subangular detrital quartz and carbonates (crystalline, bioclastic, and micritic limestones), together with bioclasts (benthic foraminiferas and echinoderm remains) and a few unweathered grains of detrital feldspars, micas, pyroxene, amphiboles, sandstones, siltstones, and oxides or hydroxides, surrounded by a calcite cement <i>Example: sample SD 23 (Fig. S2E)</i>	Coarse- to medium-grained sandstones mainly composed of subangular detrital quartz and carbonates (crystalline, bioclastic, and micritic limestones), together with bioclasts (benthic foraminiferas and echinoderm remains) and a few unweathered grains of detrital feldspars, micas, pyroxene, amphiboles, siltstones, and oxides or hydroxides, surrounded by a clay and/or micrite matrix <i>Example: sample ST 5 (Fig. S2F)</i>

28 **Table 2.** Amount of Li extracted by the water rinsing experiments (in % of bulk content).

29

Sample name	1 st rinse	2 nd rinse	3 rd rinse	Total rinsed Li	$\delta^7\text{Li}$	2 s.d.
Alluvial sediments						
SA3	0.10%	0.04%	0.03%	0.17%		
SA4	0.17%	0.06%	0.04%	0.28%		
SA6	0.23%	0.10%	0.10%	0.43%		
SA9	0.13%	0.05%	0.05%	0.23%		
SA11	0.16%	0.06%	0.05%	0.27%		
SA15	0.11%	0.05%	0.04%	0.20%		
SA22	0.12%	0.06%	0.04%	0.22%		
Seawater contacted sediments (coastal and marine)						
SC4	0.24%	0.07%	0.04%	0.35%	10.57	0.02
SC11	0.09%	0.04%	0.02%	0.15%	12.34	0.10
SC21	0.15%	0.04%	0.03%	0.22%	12.84	0.13
SD3	0.68%	0.12%	0.07%	0.87%	2.15	0.07
SD7	0.39%	0.08%	0.05%	0.52%	1.91	0.17
SD21	0.23%	0.06%	0.03%	0.32%	2.71	0.11
SD23	0.33%	0.10%	0.05%	0.48%	7.50	0.13
ST5	0.29%	0.17%	0.11%	0.57%	12.14	0.21

30

31
32

Table 3. Li isotope composition of the first and the last leach solution obtained from the HCl-leaching experiments.

Sample	First leach			Third leach		
	$\delta^7\text{Li}$	Al/Ca	Fe/Ca	$\delta^7\text{Li}$	Al/Ca	Fe/Ca
Alluvial sediments						
SA 4	3.68±0.24	3.91×10 ⁻⁶	6.97×10 ⁻⁵	-1.73 ± 0.20	9.67×10 ⁻²	5.08×10 ⁻²
SA 9	5.52±0.13	1.61×10 ⁻⁵	8.43×10 ⁻⁵	-2.28 ± 0.21	3.94×10 ⁻²	4.30×10 ⁻²
SA 11	2.60±0.07	5.29×10 ⁻⁶	6.67×10 ⁻⁵	0.13 ± 0.24	2.85×10 ⁻²	2.27×10 ⁻²
SA 15	4.61±0.10	7.30×10 ⁻⁶	6.93×10 ⁻⁵	-0.45 ± 0.26	3.45×10 ⁻²	2.56×10 ⁻²
Seawater contacted sediments (coastal and marine)						
SD 3	-0.55±0.09	3.11×10 ⁻⁵	7.51×10 ⁻⁵	-6.01 ± 0.14	6.26×10 ⁻²	1.00×10 ⁻¹
SD 7	-6.32±0.08	1.49×10 ⁻²	2.72×10 ⁻²	-3.53 ± 0.27	3.10×10 ⁻¹	3.94×10 ⁻¹
ST 5	2.88±0.22	2.29×10 ⁻⁵	8.51×10 ⁻⁵	-4.67 ± 0.37	7.80×10 ⁻²	1.95×10 ⁻¹
SC 21	6.16±0.37	1.20×10 ⁻⁵	6.60×10 ⁻⁵	-2.83 ± 0.30	3.43×10 ⁻²	2.38×10 ⁻²

33
34
35
36

S1.1 Lithium isotope measurements

A double-step separation protocol using cation exchange resin (Biorad, AG50W-X12, 200-400 mesh) was employed in order to separate Li from the sample matrix (Zhang et al., 2021). During each separation session, five reference materials (BHVO-2, JB-2, NASS-6, SRM-2709a, and TILL-1) were routinely processed together with samples to evaluate the quality of this protocol. The Li isotope composition of the purified samples was measured using a Thermo Fisher Neptune Plus MC-ICP-MS. The pure Li standard solutions IRMM-016 and SPEC were routinely used to monitor the instrumental stability, while the L-SVEC solution was used as a bracketing standard to correct for instrumental mass fractionation. Accurate and reproducible Li isotope compositions for IRMM-016 ($\delta^7\text{Li}=0.13\pm 0.17\%$, 2 SD, n=36), SPEC ($\delta^7\text{Li}=94.32\pm 0.19\%$, 2 SD, n=26), NASS-6 ($\delta^7\text{Li}=30.95\pm 0.51\%$, 2 SD, n=12), BHVO-2 ($\delta^7\text{Li}=4.66\pm 0.78\%$, 2 SD, n=11), SRM-2709a ($\delta^7\text{Li}=-0.30\pm 0.58\%$, 2 SD, n=13), TILL-1 ($\delta^7\text{Li}=6.69\pm 0.68\%$, 2 SD, n=14), and JB-2 ($\delta^7\text{Li}=4.72\pm 0.80\%$, 2 SD, n=15) were obtained. All the results are in good agreement with values reported in previous studies (Brand et al., 2014; Dellinger et al., 2014; Weynell et al., 2017; Kuessner et al., 2020).

S1.2 Silicon isotope measurements

In order to analyse the Si isotope composition, an aliquot of each crushed sample was first digested using an alkali (NaOH) fusion method (Georg et al., 2006), and the Si concentration of digested sample solution was analysed using ICP-Q-MS. Then, a widely-adopted Si separation protocol was used (Georg et al., 2006; Pringle et al., 2016) using AG50W-X12 (200-400 mesh) resin. Si isotope composition was measured on a Thermo Fisher Neptune Plus MC-ICP-MS within 24 hours after the Si separation. The well-characterized reference material BHVO-2 was routinely analysed as an external standard to check the quality of the separation protocol and of the isotope measurements. The reference material National

Bureau of Standards 28 Sand Quartz (NBS-28, or also called NIST RM-8546) was processed through the same digestion and separation methods and was used as the bracketing standard to correct for instrumental mass fractionation. The Si isotope composition is expressed in δ -notation in the unit of ‰ related to NBS-28: $\delta^x\text{Si} = [({}^x\text{Si}/{}^{28}\text{Si})_{\text{Sample}}/({}^x\text{Si}/{}^{28}\text{Si})_{\text{NBS-28}} - 1] \times 1000$, where $x=29$ or 30 . Mass-dependent fractionation of Si isotopes across all samples is indicated by the linear relationship observed between $\delta^{30}\text{Si}$ and $\delta^{29}\text{Si}$ across all samples, with a slope value of 0.5153, which is between the value of kinetic fractionation (0.5092; Young et al., 2002) and that of equilibrium fractionation (0.5178; Young et al., 2002), undistinguishable from the two fractionations. The $\delta^{30}\text{Si}$ value of BHVO-2 measured in this study ($-0.29 \pm 0.05\text{‰}$, 2 SD, $n=21$) is in agreement with previously reported values (Zambardi and Poitrasson, 2011; Savage et al., 2013).

S1.3 Neodymium isotope measurements

To separate Nd from the matrix, we have employed a double-column method (Caro et al., 2006). Sample solution was first allowed to pass a column packed with the TRU-spec resin (Eichrom) to separate rare earth elements from the sample matrix, then to pass a second column packed with the Ln-spec resin (Eichrom) to further purify Nd. Finally, Nd isotope composition was measured on a Neptune MC-ICP-MS, using a ${}^{142}\text{Nd}/{}^{144}\text{Nd}$ ratio of 0.7218 for internal correction of instrumental mass fractionation. In this study, the Nd isotope composition is expressed in ϵ -notation: $\epsilon\text{Nd} = [({}^{143}\text{Nd}/{}^{144}\text{Nd})_{\text{Sample}}/({}^{143}\text{Nd}/{}^{144}\text{Nd})_{\text{CHUR}} - 1] \times 10000$ where CHUR stands for chondritic uniform reservoir (${}^{143}\text{Nd}/{}^{144}\text{Nd} = 0.512638$). The reported results are within an analytical uncertainty estimated at ~ 0.2 ϵNd units from repeated runs of standard solutions.

- Brand, W.A., Coplen, T.B., Vogl, J., Rosner, M., and Prohaska, T., 2014, Assessment of international reference materials for isotope-ratio analysis (IUPAC Technical Report): *Pure and Applied Chemistry*, v. 86, p. 425–467.
- Caro, G., Bourdon, B., Birck, J.-L., and Moorbath, S., 2006, High-precision $^{142}\text{Nd}/^{144}\text{Nd}$ measurements in terrestrial rocks: constraints on the early differentiation of the Earth's mantle: *Geochimica et Cosmochimica Acta*, v. 70, p. 164–191.
- Dellinger, M., Gaillardet, J., Bouchez, J., Calmels, D., Galy, V., Hilton, R.G., Louvat, P., and France-Lanord, C., 2014, Lithium isotopes in large rivers reveal the cannibalistic nature of modern continental weathering and erosion: *Earth and Planetary Science Letters*, v. 401, p. 359–372, doi:<http://dx.doi.org/10.1016/j.epsl.2014.05.061>.
- Georg, R.B., Reynolds, B.C., Frank, M., and Halliday, A.N., 2006, New sample preparation techniques for the determination of Si isotopic compositions using MC-ICPMS: *Chemical Geology*, v. 235, p. 95–104, doi:<http://dx.doi.org/insu.bib.cnrs.fr/10.1016/j.epsl.2006.07.006>.
- Kuessner, M.L., Gourgiotis, A., Manhès, G., Bouchez, J., Zhang, X., and Gaillardet, J., 2020, Automated Analyte separation by Ion Chromatography using a Cobot Applied to Geological Reference Materials for Li Isotope Composition: *Geostandards and Geoanalytical Research*, doi:10.1111/ggr.12295.
- Pringle, E.A., Moynier, F., Savage, P.S., Jackson, M.G., Moreira, M., and Day, J.M.D., 2016, Silicon isotopes reveal recycled altered oceanic crust in the mantle sources of Ocean Island Basalts: *Geochimica et Cosmochimica Acta*, v. 189, p. 282–295, doi:<http://dx.doi.org/insu.bib.cnrs.fr/10.1016/j.gca.2016.06.008>.
- Savage, P.S., Georg, R.B., Williams, H.M., and Halliday, A.N., 2013, The silicon isotope composition of the upper continental crust: *Geochimica et Cosmochimica Acta*, v. 109, p. 384–399, doi:<http://dx.doi.org/10.1016/j.gca.2013.02.004>.

- Weynell, M., Wiechert, U., and Schuessler, J.A., 2017, Lithium isotopes and implications on chemical weathering in the catchment of Lake Donggi Cona, northeastern Tibetan Plateau: *Geochimica et Cosmochimica Acta*, v. 213, p. 155–177, doi:<https://doi.org/10.1016/j.gca.2017.06.026>.
- Young, E.D., Galy, A., and Nagahara, H., 2002, Kinetic and equilibrium mass-dependent isotope fractionation laws in nature and their geochemical and cosmochemical significance: *Geochimica et Cosmochimica Acta*, v. 66, p. 1095–1104.
- Zambardi, T., and Poitrasson, F., 2011, Precise Determination of Silicon Isotopes in Silicate Rock Reference Materials by MC-ICP-MS: *Geostandards and Geoanalytical Research*, v. 35, p. 89–99.
- Zhang, X. (Yvon) et al., 2021, Experimental constraints on Li isotope fractionation during the interaction between kaolinite and seawater: *Geochimica et Cosmochimica Acta*, v. 292, p. 333–347, doi:<https://doi.org/10.1016/j.gca.2020.09.029>.

Supplementary figures

Figure S1. Examples of sedimentological sections representative of deposits from the different environments sampled through the deltaic complex in the Ainsa Basin.

Figure. S2 Pictures of thin sections representative of deposits from the different environments sampled through the deltaic complex in the Ainsa Basin. These pictures were taken with an optical microscope using plane-polarized light above and cross-polarized light below.

Figure S3. Relationship between Li concentration and the total contents of Al and Fe.

Figure S4. Concentrations of Ca, Li, Al, and Fe in solutions from sequential HCl-leaching experiment performed on alluvial (displayed in red) and seawater-contacted (displayed in blue) sediments from the Ainsa Basin.

Figure S5. $\delta^7\text{Li}$ values of the bulk samples and the solutions from the first (carbonate-bound Li) and third (Al–Fe associated Li) steps of the HCl-leaching experiments. The color code for alluvial, marine, and coastal samples the same as in Figure S3.

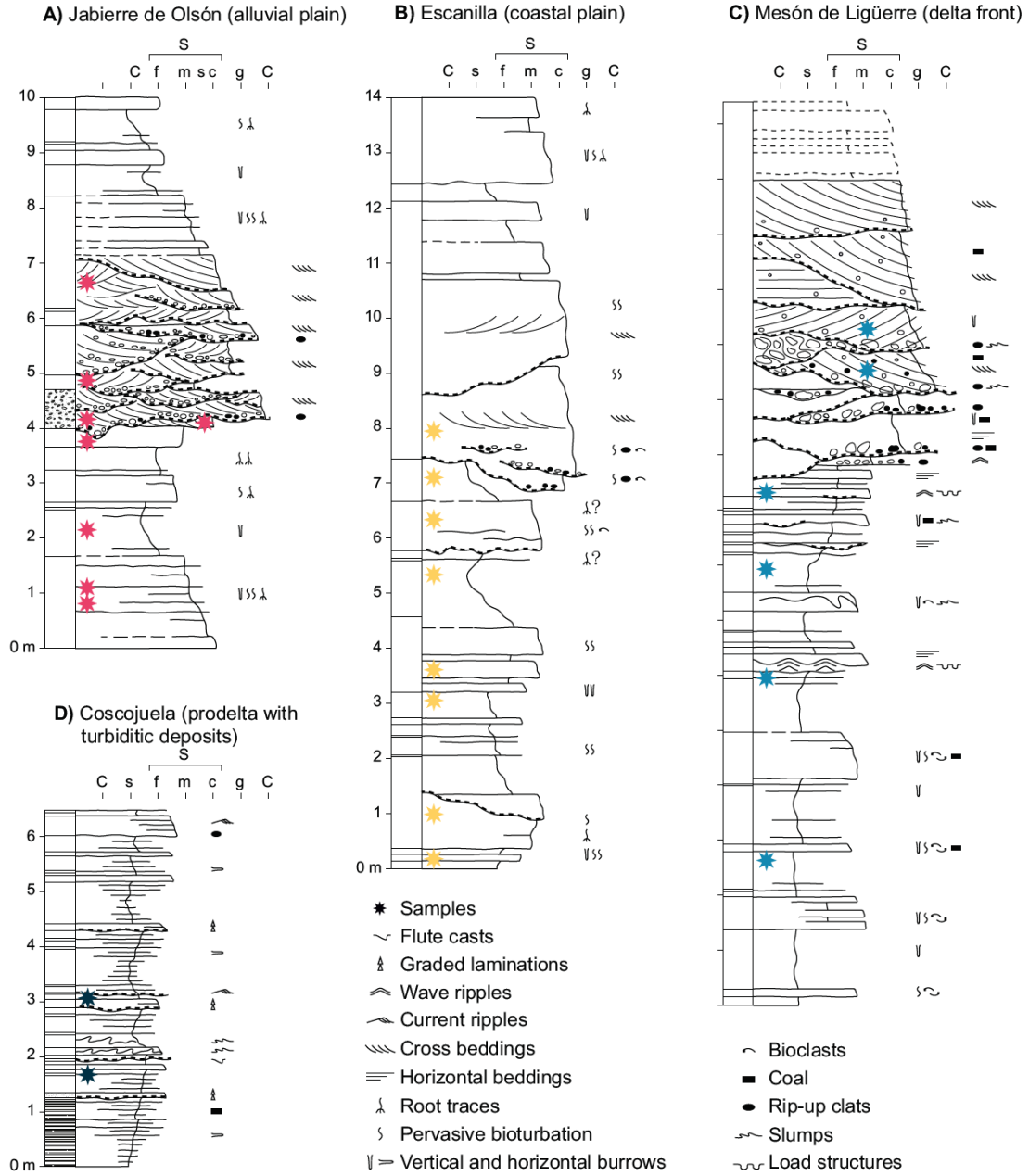


Figure S1

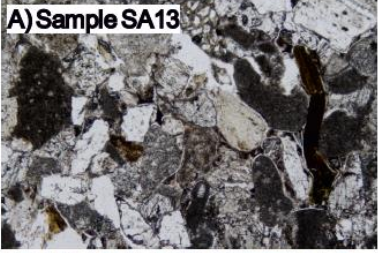
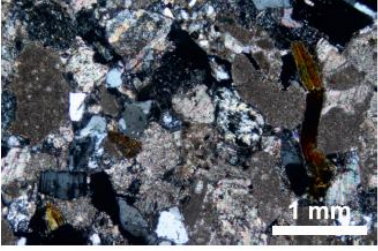
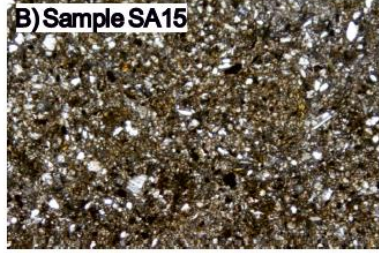
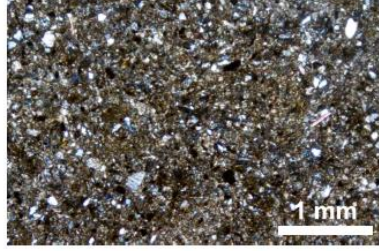
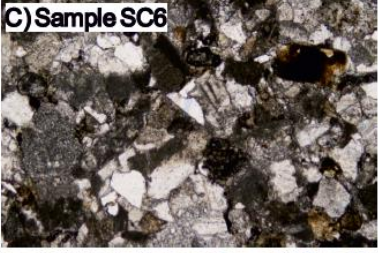
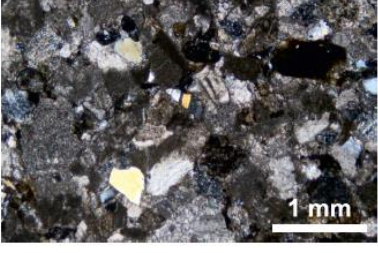
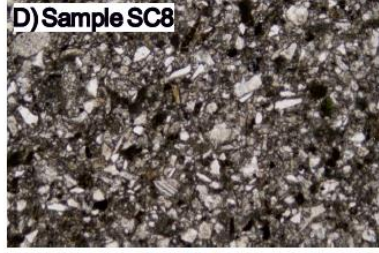
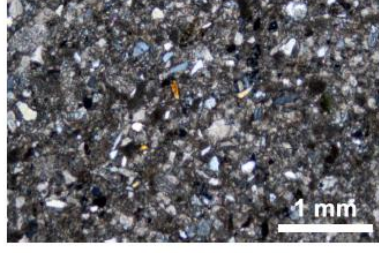
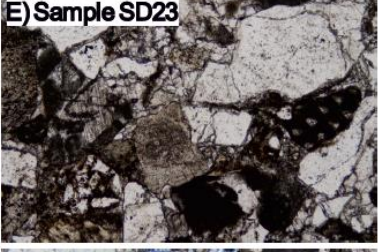
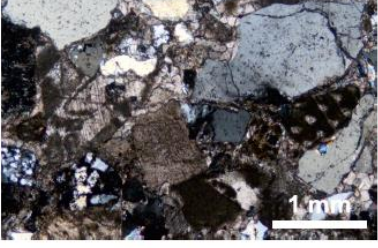
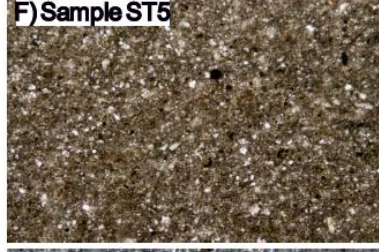
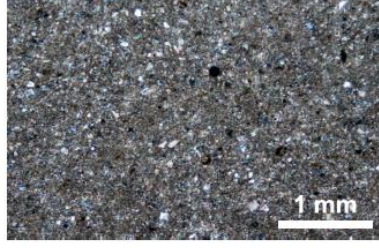
<i>Depositional environment</i>	<i>Coarse fraction</i>	<i>Fine fraction</i>
Alluvial	<p data-bbox="584 282 766 313">A) Sample SA13</p>  	<p data-bbox="983 282 1165 313">B) Sample SA15</p>  
Coastal	<p data-bbox="584 819 750 851">C) Sample SC6</p>  	<p data-bbox="983 819 1149 851">D) Sample SC8</p>  
Marine	<p data-bbox="584 1357 762 1388">E) Sample SD23</p>  	<p data-bbox="983 1357 1149 1388">F) Sample ST5</p>  

Figure S2

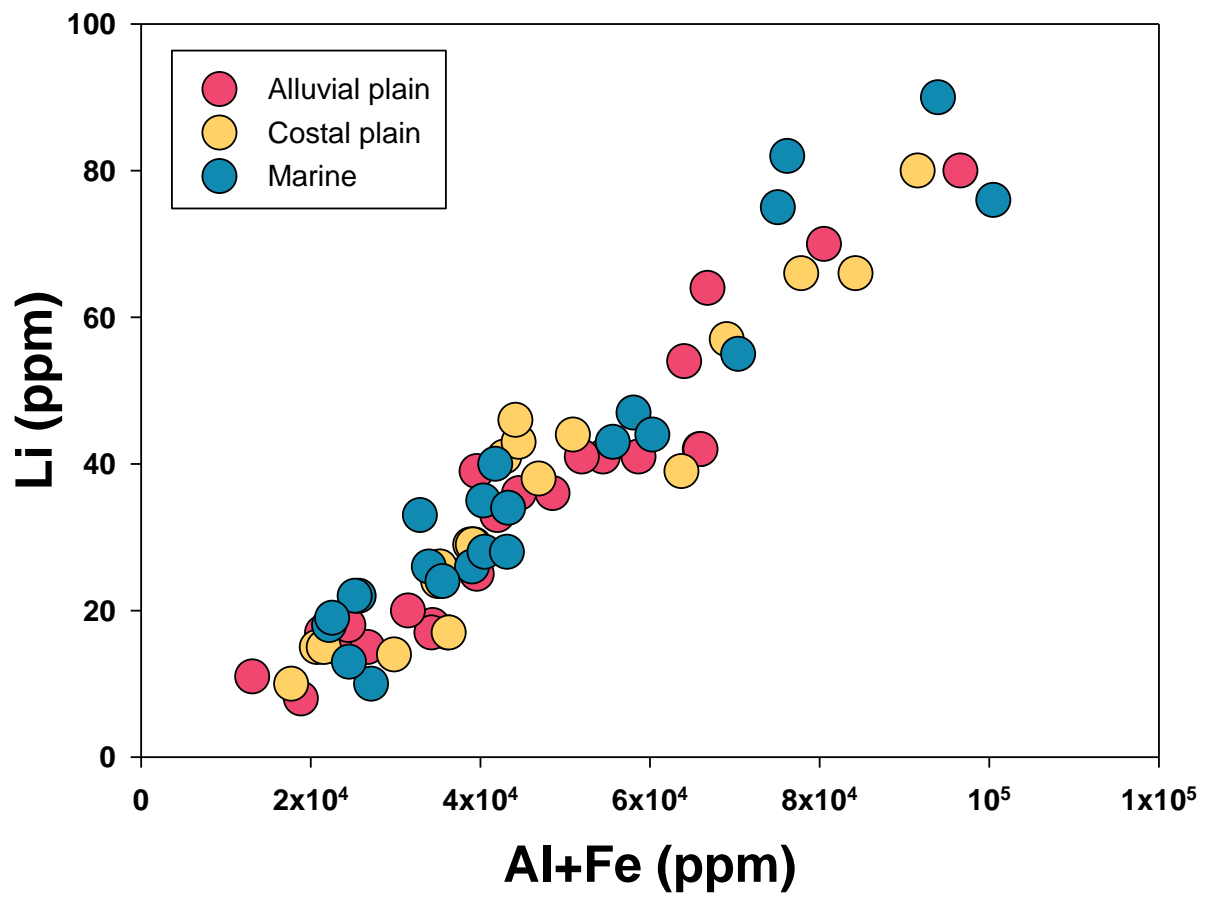


Figure. S3

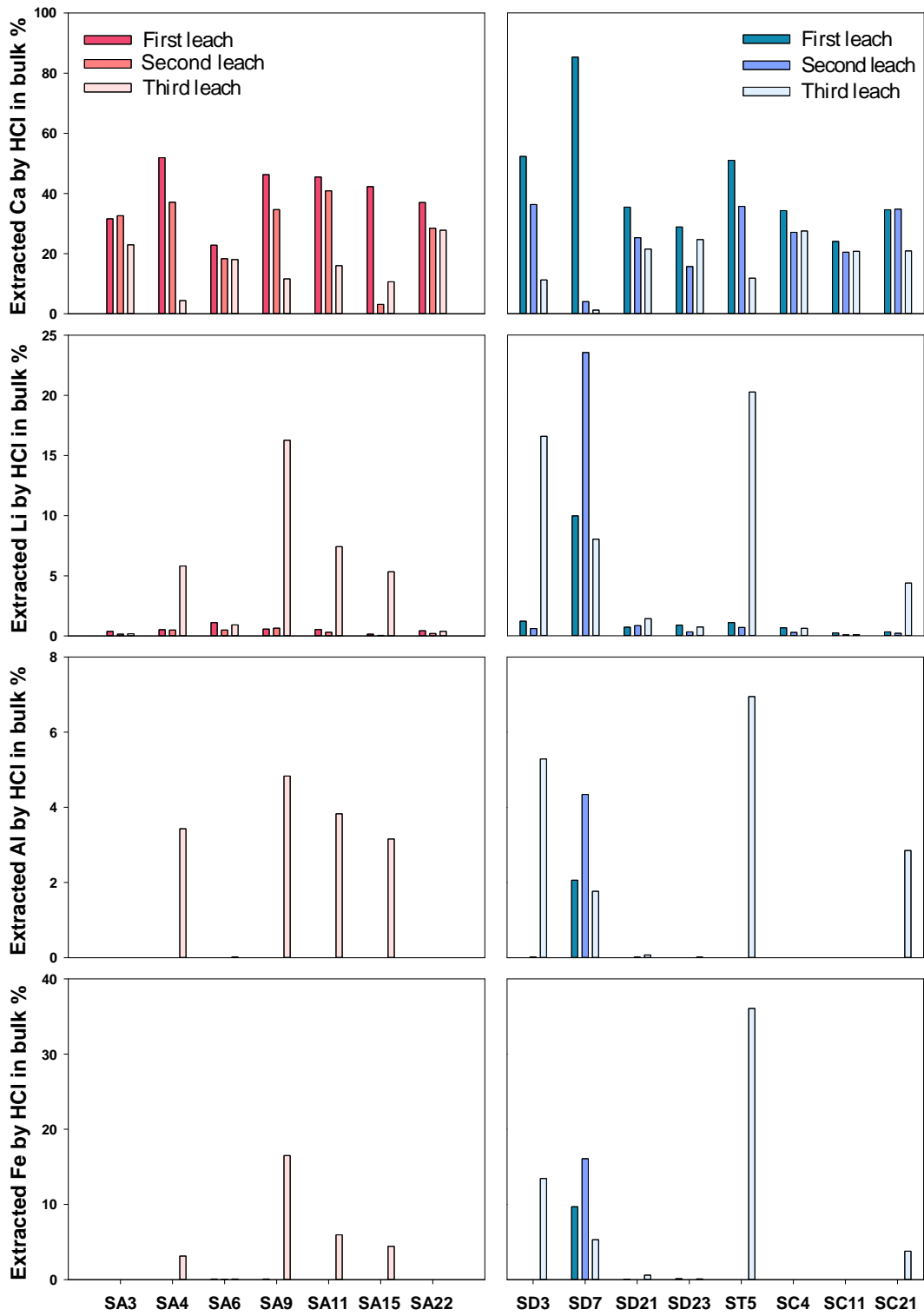


Figure S4

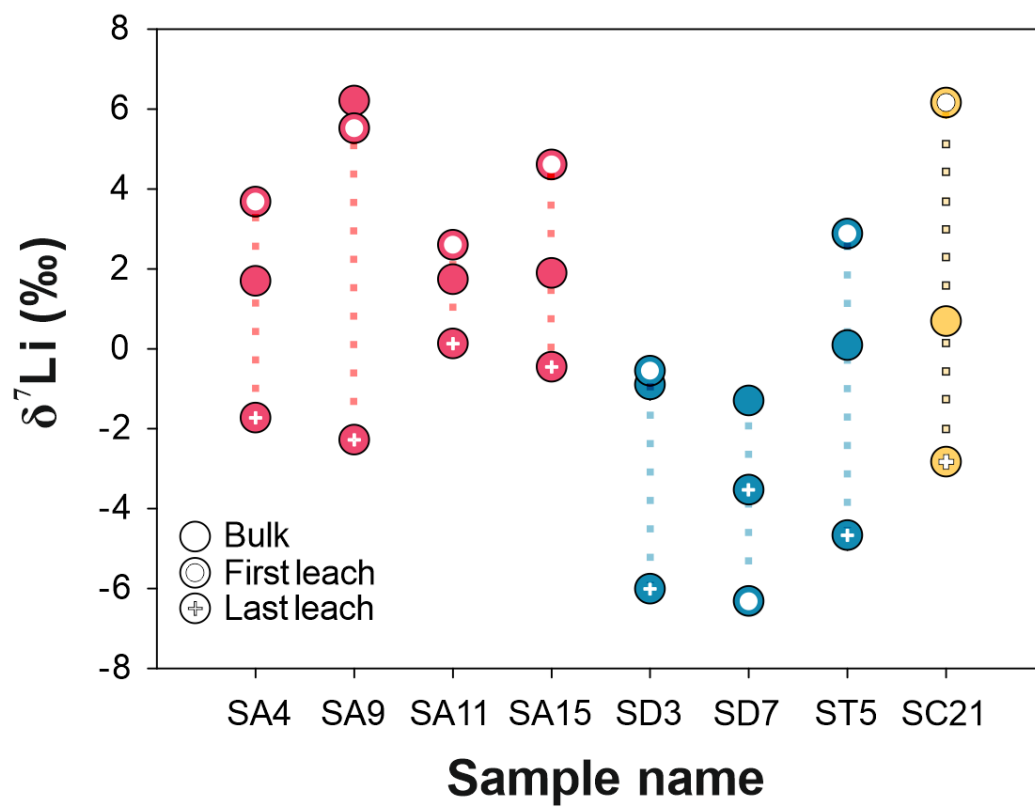


Figure S5